UNIVERSITY OF BIRMINGHAM

Analysis of pressure field generated by a collapsing bubble

Li, S.; Han, R.; Zhang, A. M.; Wang, Qianxi

[Link to publication on Research at Birmingham portal](#)

Analysis of pressure field generated by a collapsing bubble

Shuai Li [a], Rui Han[a], Aman Zhang [a,†], Qianxi Wang [b]

[a]College of Shipbuilding Engineering, Harbin Engineering University, Harbin, P.R. China

[b]School of Mathematics, The University of Birmingham, B15 3TT, United Kingdom

This paper is concerned with the dynamic pressure induced by a collapsing bubble, based on the potential flow theory coupled with the boundary element method. The pressure is calculated using the Bernoulli equation, where the partial derivative of the potential in time is calculated using the auxiliary function method. The numerical results agree well with experimental results, in terms of bubble shape and pressure fields. There are two root causes of the bubble induced pressure and the dynamic pressure is decomposed into two parts correspondingly. The first part p_g is associated with the imbalanced pressure between the bubble gas and the ambient flow, which measures the contribution of the high pressure gas to the dynamic pressure. The second part p_m is caused by the bubble motion, which helps evaluate the contribution of the jet impact. The variation of p_g has the same pattern with the gas pressure. p_m at the wall center reaches its first peak soon after the jet impact, and then decreases due to the reduction of jet velocity. As the toroidal bubble migrates towards the wall, p_m may rise again. We also investigate the influences of dimensionless parameters on the pressure field induced by a gas/cavitation bubble.

Keywords: Bubble dynamics; cavitation; dynamic pressure; jet impact; boundary element method

1.   Introduction

Bubble dynamics are associated wide applications in industrial systems: cavitation on ship propellers and hydroturbines (Choi et al., 2009; Hsiao et al., 2012), seabed geophysical exploration (Graaf et al., 2014), underwater explosion (Klaseboer et al., 2005; Wang, 2013; Liu et al., 2014), and ultrasonic cleaning (Song et al., 2004;

Wijngaarden, 2015; Chahine et al., 2015; Ohl et al., 2006). Analyses of the pressure fields generated by a collapsing bubble are directly associated with the mechanism of erosion, underwater explosion, etc.

Rayleigh (1917) theoretically demonstrated that a local high pressure will be generated during the collapse phase of a spherical symmetrical bubble. The pressure can be very high and consequently leads to an outgoing shock wave (Harrison, 1952). However, the bubble cannot keep spherical when affected by gravity (Zhang et al., 2015a), interacts with a shock wave (Klaseboer et al., 2006), near a free surface (Blake and Gibson, 1981) or near a rigid boundary (Naude and Ellis, 1961). The pressure field surrounding a non-spherical bubble is quite different from a spherical one. The jet formation is the main feature of a non-spherical bubble.

For a bubble collapsing near a rigid wall, there is a high pressure region located behinds the jet during collapse (Blake et al., 1986; Best and Kucera, 1992; Zhang et al., 1993; Brujan et al., 2002). After jet impact, another high pressure region is located ahead of the bubble (Best and Kucera, 1992). Two high local peak pressures were predicted by Blake et al. (1997): The earlier one is associated with jet impact, while the later one coincides with the large internal pressures of the bubble at minimum volume. Philipp and Lauterborn (1998) also observed two individual shock waves during the bubble collapse in some experiments. The first shock wave is generated by the impact of the jet tip onto the opposite bubble wall. The second shock wave emitted when the bubble reaches its minimum volume. Until now, two characteristic effects are believed to be mainly responsible for the destructive action: the high pressure pulse (when bubble reaches its minimum volume) and the high-speed liquid jet impact.

In all, the bubble induced pressure is a combination of the high pressure gas (around minimum volume) and the high-speed fluid motion (jet, splash, rebound, etc.). The correlate mechanisms will offer the reference for the above applications. For example, if the jet impact dominates the erosion process, we should take actions to prevent the jet or change the jet direction (Brujan et al., 2001; Gibson and Blake, 1982; Duncan and Zhang, 1991). If the gas pressure plays an important role in cleaning, we should enhance the compression of the bubble gas. Actually, it is difficult to divide the two effects apart in experiments. However, theoretical or numerical studies could yield a valuable contribution to the clarification of the influences of these two factors on the above applications.

Given this, the dynamic pressure induced by a non-spherical bubble is decomposed into two parts theoretically in present study: the first one is caused by the bubble gas pressure and the second one is induced by the bubble motion. Both these two sub-pressures have specific physical meanings, which helps evaluate the gas induced pressure and the jet impact pressure, respectively. For a cavitation bubble with its inner pressure keeps vapor pressure, this pressure decomposition is also implemented and a comparison is made with a gas bubble.

In numerical calculation, boundary element/integral method (BEM/BIM) is used to simulate the bubble motion. BEM was extensively and successfully applied to bubble dynamics, which was validated by a large number of experiments (Tong et al., 1999; Robinson et al., 2001; Dadvand et al., 2011; Wang, 2014; Zhang et al., 2015b; Han et al., 2015). The vortex ring model (Wang et al. 1996; Zhang and Liu, 2015) is adopted to handle the discontinuous velocity potential on a toroidal bubble surface, and a multiple vortex rings model (Zhang et al., 2015b) is used after the splitting of a toroidal bubble. Besides, an auxiliary function method is adopted to calculate the total dynamic pressure and two sub-pressures.

An underwater explosion bubble experiment in literature are used to validate our numerical model, and the experimental and numerical results meet well, in terms of bubble shape evolutions and pressure signals. We also conduct a spark-generated bubble experiment, and the corresponding numerical analysis is made, in which the characteristics of the decomposed pressures are analyzed. At last, the effects of the stand-off parameter, the strength parameter and the ratio of the specific heats for the gas are discussed.

2.   Theory and numerical method_{Equation Chapter 1 Section 1Equation Section 2}

2.1   Basic formulas

Consider bubble dynamics in an axisymmetric configuration. A cylindrical coordinate system $O - r\theta z$ is adopted in our model. The origin is placed at the initial bubble center and z axis is pointing towards the opposite direction of the gravity acceleration.

Because of the high velocities and consequent high Reynolds number during the growth and collapse of a bubble, viscosity is found to play a negligible role in the

collapse of a cavitation bubbles. For bubbles in a very viscous fluid (more than thousands of time the viscosity of water), the viscosity would slow down the collapse process (Tinguely, 2013; Brujan and Matsumoto, 2014). In the present study, the flow surrounding the bubble is assumed inviscid, incompressible and irrotational. The velocity potential φ satisfies the following boundary integral equation:

$$\lambda(\mathbf{r},t)\varphi(\mathbf{r},t) = \iint_S \left[\frac{\partial\varphi(\mathbf{q},t)}{\partial n} G(\mathbf{r},\mathbf{q}) - \varphi(\mathbf{q},t)\frac{\partial}{\partial n} G(\mathbf{r},\mathbf{q}) \right] dS, \tag{2.1}$$

where $\mathbf{r}$ is the field point and $\mathbf{q}$ is the source point, $\lambda(\mathbf{r},t)$ is the solid angle, S includes all the boundaries of the flow domain, $\partial/\partial n$ is the normal outward derivative from the boundary. When dealing with a bubble near an infinite rigid wall, the Green function $G(\mathbf{r},\mathbf{q})$ is taken as

$$G(\mathbf{r},\mathbf{q}) = \frac{1}{|\mathbf{r}-\mathbf{q}|} + \frac{1}{|\mathbf{r}-\mathbf{q}'|}, \tag{2.2}$$

where $\mathbf{q}'$ is the reflected image of $\mathbf{q}$ across the rigid wall.

The kinematic boundary condition and dynamic boundary condition on bubble surface are as follows:

$$\frac{d\mathbf{r}}{dt} = \nabla\varphi, \tag{2.3}$$

$$\frac{d\varphi}{dt} = \frac{|\nabla\varphi|^2}{2} + \frac{p_\infty}{\rho} - \frac{p_b}{\rho} - gz, \tag{2.4}$$

where p_b is the bubble gas pressure, p_∞ is the ambient pressure of the liquid at the inception point of the bubble, ρ is the density of the liquid, g is the gravity acceleration.

Assuming that the expansion and contraction of the bubble gas are adiabatic, the gas pressure inside the bubble is expressed as follows:

$$p_b = p_c + p_{ini}(V_{ini}/V)^\kappa, \tag{2.5}$$

where V is the bubble volume, the subscript ini denotes initial quantities, κ is the ratio of the specific heats for the gas, p_c is the vapor pressure. Surface tension is neglected in this study for the large Weber number ($We \sim 10^4$) during the growth and collapse of a bubble. For bubbles with a radius of the order of micrometer, the effect of surface tension is not negligible anymore (Tinguely, 2013).

Bubble is transformed from a singly-connected into a double-connected form after

the jet impact upon the opposite bubble surface, and there exists a velocity potential jump at the impact point. Wang et al. (1996, 2005) introduced a vortex ring inside the toroidal bubble to handle this problem. The vortex ring model has been widely used to simulate the toroidal bubble motion, which is not introduced in detail.

The splitting of a toroidal bubble near a rigid boundary is commonly seen in experiments. In our previous paper (Zhang et al., 2015b), the multiple vortex rings model is established to simulate the interaction between two toroidal bubbles near a rigid boundary. A brief description about this model is made as follows.

Two vortex rings are placed inside the two toroidal bubbles respectively. The velocity potential in the flow is decomposed as follows:

$$\varphi = \varphi_{vr1} + \varphi_{vr2} + \varphi_{vr\_m1} + \varphi_{vr\_m2} + \phi, \tag{2.6}$$

where φ_{vr} is the induced potential by the vortex ring, φ_{vr_m} is the induced potential by the mirror vortex ring (reflection of the vortex ring across the rigid wall), ϕ is the single-valued remnant potential.

The velocity in the flow is also decomposed into five parts:

$$\boldsymbol{u} = \boldsymbol{u}_{vr1} + \boldsymbol{u}_{vr2} + \boldsymbol{u}_{vr\_m1} + \boldsymbol{u}_{vr\_m2} + \nabla \phi, \tag{2.7}$$

where the first four terms are induced velocities by the vortex rings, which can be calculated by the Biot-Savart law. The last part $\nabla \phi$ is induced by remnant potential, which can be calculated using BEM. More details about multiple vortex rings model refers to Zhang et al. (2015b).

Assume the initial bubble has a spherical shape and the velocity on bubble surface is zero. At each time step, the bubble surface and the velocity potential on it are known. We can use these informations to calculate the tangential velocity using finite differential method. The normal velocity is obtained by solving the boundary integral equation. The forward time integrations of equation (2.3)-(2.4) are carried out using the fourth-order Runge-Kutta method.

2.2   Pressure calculation

The pressure distribution p in the flow field can be evaluated using Bernoulli equation:

$$p = p_\infty - \rho gz - \rho(\frac{\partial \varphi}{\partial t} + \frac{|\nabla \varphi|^2}{2}). \tag{2.8}$$

Best (1991) and Dawoodian et al. (2015) employed the finite difference approximation to calculate (2.8). However, this method needs several velocity potentials at different time steps, which is not accurate enough. In present study, a more precise approximation is used, which is called the auxiliary function method (Duncan et al., 1996; Wu and Hu, 2004).

The auxiliary function Ψ is defined as:

$$\Psi = \frac{\partial \varphi}{\partial t}. \tag{2.9}$$

It is noted that the term $\partial \varphi / \partial t$ also satisfies Laplace equation (Duncan et al., 1996; Wu and Hu, 2004):

$$\nabla^2 \Psi = 0. \tag{2.10}$$

The auxiliary function Ψ has the similar mathematical properties with velocity potential. On the bubble surface, Ψ satisfies:

$$\Psi = \frac{p_\infty - p_b}{\rho} - \frac{|\nabla \varphi|^2}{2} - gz. \tag{2.11}$$

The source density ω is defined here, which is continuously distributed on bubble surface (Wang et al., 2004):

$$\psi(\boldsymbol{r}) = \iint_S \frac{\omega(\boldsymbol{q})}{|\boldsymbol{r} - \boldsymbol{q}|} dS. \tag{2.12}$$

In numerical computation, Eq. (2.12) transforms into:

$$\psi(\boldsymbol{r}) = \iint_S \frac{\omega(\boldsymbol{q})}{|\boldsymbol{r} - \boldsymbol{q}|} dS = [G] \cdot \omega(\boldsymbol{q}) \tag{2.13}$$

We let $\boldsymbol{r}$ be on the boundary (bubble surface), the source density can be obtained through $\omega(\boldsymbol{q}) = [G]^{-1} \cdot \psi(\boldsymbol{r})$, as $[G]$ is obtained when solving Eq. (2.1) and $\psi(\boldsymbol{r})$ can be easily obtained by Eq. (2.11). The requirements on memory and coding efforts in calculating $\omega(\boldsymbol{q})$ are insignificant. Then, the value of Ψ in the flow field induced by all the sources can be evaluated by the integration over the bubble surface.

2.3 Pressure decomposition

The pressure field p consists of dynamic pressure p_d and the static pressure p_s.

The dynamic pressure p_d is divided into two parts: p_g and p_m associated with the gas pressure and bubble motion, respectively:

$$p = p_d + p_s = p_g + p_m + p_s.$$ (2.14)

In order to decompose the pressure in the flow domain into three parts, the auxiliary function Ψ on bubble surface is also divided into three parts:

$$\Psi = \Psi_g + \Psi_m + \Psi_s,$$ (2.15)

where

$$\Psi_g = \frac{p_\infty - p_b}{\rho}, \qquad \Psi_m = -\frac{(\nabla \varphi)^2}{2}, \qquad \Psi_s = -gz.$$ (2.16)

Ψ_g, Ψ_m, Ψ_s are associated with the pressure difference between the gas and the ambient flow, the bubble motion, and gravity, respectively.

Three source densities are obtained by substituting (2.16) into (2.12).

$$\omega = \omega_g + \omega_m + \omega_s.$$ (2.17)

Thus, the pressure field and three sub-pressures can be expressed as follows:

$$p = p_\infty - \rho(\iint_S \frac{\omega(q)}{|r-q|} dS + \frac{|\nabla \varphi|^2}{2}) - \rho gz,$$ (2.18)

$$p_s = p_\infty - \rho gz,$$ (2.19)

$$p_g = -\rho \iint_S \frac{\omega_g(q)}{|r-q|} dS,$$ (2.20)

$$p_m = -\rho(\iint_S \frac{\omega_m(q)}{|r-q|} dS + \frac{|\nabla \varphi|^2}{2}).$$ (2.21)

The above three decomposed pressures have specific physical meaning and analytic expressions. In particular, p_g can be used to evaluate the pulsating pressure during the collapse phase of a gas bubble, and p_m can be used to evaluate impact pressure from a liquid jet.

If there are n toroidal bubbles near a rigid boundary, the term $\partial \varphi / \partial t$ is decomposed into $2n+1$ parts:

$$\frac{\partial \varphi}{\partial t} = \sum_{i=1}^{n} \frac{\partial \varphi_{vri}}{\partial t} + \sum_{i=1}^{n} \frac{\partial \varphi_{vr\_mi}}{\partial t} + \frac{\partial \phi}{\partial t}.$$ (2.22)

The last term $\partial \phi / \partial t$ can be obtained from the same method introduced above. As

the position of the vortex rings can be treated as fixed in the current time step, the first two terms on the right side of (2.22) equals zero. After the decomposition of the term $\partial\phi/\partial t$, the sub-pressures in (2.19)-(2.21) can also be obtained.

In the following discussion, we have scaled length with respect to the equivalent maximum radius of the bubble R_m; and pressure with p_∞; and density with ρ. Besides, three dimensionless parameters are introduced to describe the initial condition of a bubble:

$$\varepsilon = p_{ini} \,/\, p_\infty\,, \quad \gamma = d\,/\,R_m\,, \quad \delta = \sqrt{\rho g R_m \,/\, p_\infty}\,. \tag{2.23}$$

The initial pressure inside the bubble can be described by strength parameter ε; the distance between the bubble center and the rigid wall is described by stand-off parameter γ; the buoyancy effect of the bubble is described by buoyancy parameter δ. In addition, if the maximum dimensionless bubble radius is expected to reach 1 in calculation, the initial bubble radius R_{ini} satisfies:

$$\varepsilon(R_{ini}^{3\kappa} - R_{ini}^3) = (\kappa - 1)(R_{ini}^3 - 1). \tag{2.24}$$

3.   Results and discussion Equation Section (Next)

In Section 3.1, comparisons are made between experimental and numerical results, which validate our numerical model. In Section 3.2, a spark generated bubble experiment is conducted, and the corresponding numerical analysis is made, in which the characteristics of the decomposed pressures are analyzed. Then, the effects of the stand-off parameter, the strength parameter and the ratio of the specific heats are discussed in Section 3.3, Section 3.4 and Section 3.5, respectively. At last, the pressure induced by a cavitation bubble is also investigated in Section 3.6.

3.1   Validation

The validation case is an underwater explosion bubble experiment conducted by Zhang et al. (2013a). The charge of 4.5 g PETN is used with its depth 1 m. A pressure sensor is installed at the same depth as the charge and 0.4 m away from the charge center. The maximum bubble radius is about 0.27 m, and the oscillation time is about

45 ms. The TNT equivalent of PETN in weight is taken as 1.28. The initial bubble depth is about 3.7 R_m, so the free surface will keep flat during the first period of the bubble (Zhang et al., 2012). In order to take the free surface effect into consideration, the Green function is taken as:

$$G(\boldsymbol{r}_i, \boldsymbol{r}_j) = \frac{1}{\left|\boldsymbol{r}_i - \boldsymbol{r}_j\right|} - \frac{1}{\left|\boldsymbol{r}_i - \boldsymbol{r}_j'\right|}, \tag{3.1}$$

where $\boldsymbol{r}_j'$ is the reflected image of $\boldsymbol{r}_j$ across the free surface. Other dimensionless parameters are taken as: $\varepsilon = 559$, $\delta = 0.155$. 3
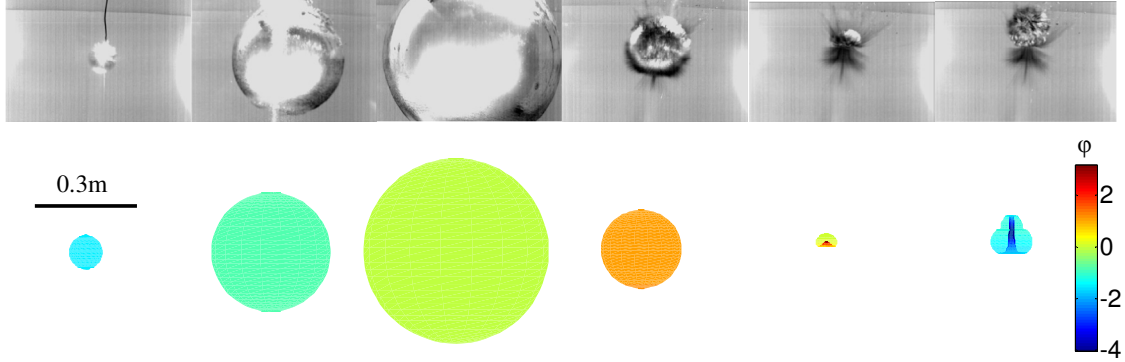

Fig. 1. Comparison between experimental (Zhang et al., 2013a) and numerical results. The charge is 4.5g PETN, detonated at the depth of 1m. A pressure sensor is placed at the same depth as the charge and 0.4m away from the charge center. The times are 0.25ms, 4.27ms, 21.6ms, 43.7ms, 44.7ms and 45.4ms, respectively.

The numerical results of bubble shapes are compared with the experimental images in Fig. 1 at typical time steps. The experimental and numerical results are shown in the first and second row respectively. In the numerical results, the contour is for the velocity potential. Each sequence shows the bubble formation (frame 1), expansion (frame 2), at maximum volume (frame 3), during collapse (frame 4), jetting (frame 5) and the toroidal bubble phase (frame 6). The computational results of the bubble shapes agree well with the experimental images.
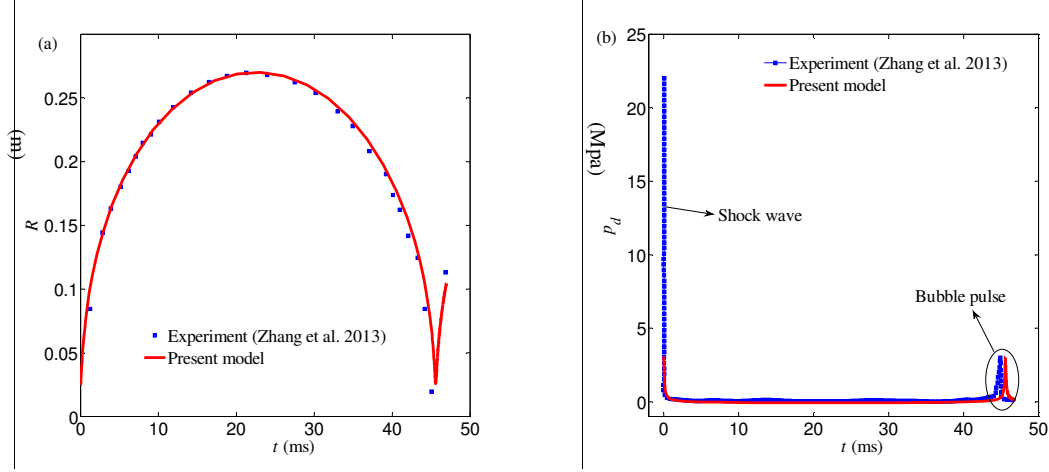
Fig. 2. Comparison between numerical result and experimental result (Zhang et al., 2013a) for an underwater explosion bubble. The parameters are the same as in Fig. 1. (a) bubble radius; (b) dynamic pressure at the testing point.

Fig. 2 shows the variations of bubble radius and the pressure signal at the testing point versus time. Firstly, the numerical result of equivalent bubble radius meets the experiment well, as shown in Fig. 2(a). Secondly, the pressure signal captured by the sensor contains the shock wave and the bubble pulse, as shown in Fig. 2(b). The present numerical model only simulates the bubble stage. It is clear that the bubble pulses of experimental and numerical results are almost identical except for a little difference in time. As discussed above, the main features of bubble shape evolution and pressure field can be reproduced by the computation.

3.2 Analysis of the two decomposed pressures

Firstly, an experiment is conducted based on the low-voltage spark bubble generation method (Turangan et al., 2006; Dadvand et al., 2009). The bubble is generated by burning the copper wire with its diameter about 0.25 mm, and captured by the Phantom V12.1 high-speed camera. The camera works at 20000 frames per second with exposure time 49 μs. Besides, the whole experiment section is illuminated from the back with a 2 kW light. More detailed information about the experiment method refers to (Zhang et al., 2013b). In the following case, the

10

maximum radius of the bubble is about 16.6 mm, the depth of the initial bubble is 200 mm and the distance between the initial bubble and the rigid boundary is 16.5 mm.
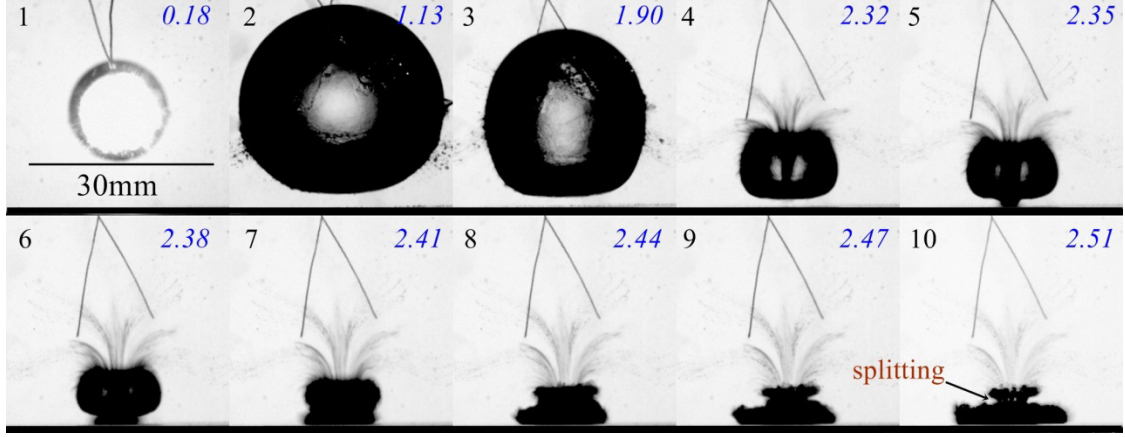

Fig. 3. High-speed photographs of bubble dynamics near a rigid boundary with $\gamma = 1$. The frame number is marked at the top-left corner of each frame, and the capturing times (dimensionless) are marked in italic at the top-right corner, and the location of the rigid boundary is the lower limit of the frames.

Some typical phenomena of the experiment are shown in Fig. 3. Each sequence shows the bubble expansion (frame 1), at maximum volume (frame 2), during collapse phase (frame 3), jet towards the wall (frame 4), the toroidal bubble phase (frame 5~8) and toroidal bubble splitting (frame 9~10). These phenomena can be divided into three phases, namely, the pre-toroidal bubble phase, the toroidal bubble phase and the toroidal bubble splitting phase.

According to the experiment, the stand-off parameter in calculation is set as 1, the buoyancy parameter is set as 0.04. The strength parameter is hard to determine because the initial pressure inside the bubble is unknown. However, a satisfying result can be achieved if we set $\varepsilon = 50$ in this case and the effect of ε will be discussed in Section 3.4.

3.2.1 Pre-toroidal bubble phase

The numerical results of the pre-toroidal bubble phase are shown in Fig. 4. These four moments are corresponding to the first four frames in Fig. 3, respectively. The pressure contours and the velocity fields are shown in the left column. The two

decomposed pressure contours (p_g and p_m) are shown in the right column, on the left-half part and right-half part respectively.
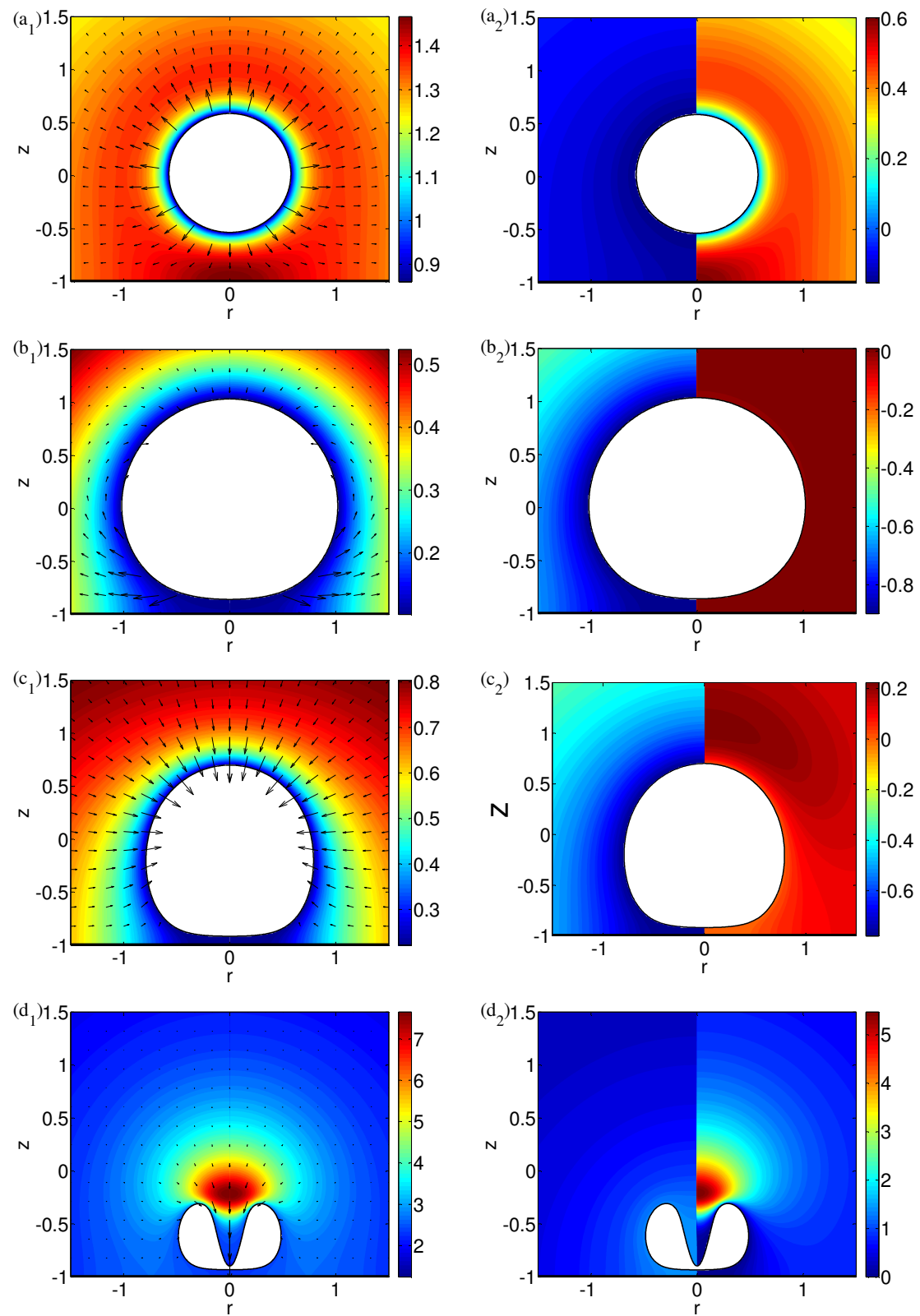

Fig. 4. Pre-toroidal bubble dynamics nearby a rigid boundary for $\varepsilon = 50$, $\gamma = 1$, $\delta = 0.04$.

The nondimensional times are 0.18, 1.13, 1.90 and 2.32, respectively. The location of the rigid boundary is the lower limit of the frames. The contours in left column represent p, and the right column represents p_g (on the left-half part) and p_m (on the right-half part).

Firstly, the pressure and velocity fields are analyzed, as shown in the left column of Fig. 4. During the expansion phase of the bubble (frame a_1), the pressure is almost symmetrically distributed under all rotations about its center, except for a slightly enhancement between the bubble and the rigid wall. The lower bubble surface is flattened by the rigid wall when it reaches its maximum volume (frame b_1). It is observed from the velocity vectors that the lower part of bubble is still expanding while the upper part begins to collapse. The bubble gas pressure (p_b) is much lower than ambient pressure (p_∞) at this moment, so the whole bubble will collapse afterwards. During the collapse phase, the radial flow directed towards the collapsing bubble will be retarded by the rigid boundary. Besides, the pressure above the bubble is higher than the near-wall region (frame c_1). Therefore, the upper part of the bubble collapses faster than the lower part, results in the formation of a high-speed liquid jet. As shown in frame d_1, the jet threads the bubble at later stage of the collapse, and the high pressure region above the bubble becomes more obvious.

In the right column of Fig. 4, the decomposed pressure p_g is shown on the left-half part. Inferred from the mathematical definition of p_g, the value of p_g on bubble surface equals the difference between p_b and p_∞. As for the first three moments (frame a_2-c_2), p_b is lower than p_∞, thus p_g is negative. In frame d_2, p_g becomes positive since p_b has exceeded p_∞. Besides, the isobaric lines of p_g are distributed surrounding the bubble surface. The pressure between the bubble and the rigid wall is enhanced when $p_b > p_\infty$ and weakened when $p_b < p_\infty$. Meanwhile, the decomposed pressure p_m is shown on the right-half part. Derived from the mathematical definition of p_m, the value of p_m on bubble surface equals zero, and being positive in the flow field, as shown in frames a_2-d_2. At the early expansion stage of the bubble (frame a_2), the liquid is pushed radial outward. However, there exists a stagnation point at the wall center due to the zero flux condition. Thus, a high pressure region forms between the bubble and the wall. In frame b_2, the bubble reaches its maximum volume and is almost motionless, so p_m in the flow approaches zero. In frame c_2, an obviously high pressure region appears above the

bubble. This is because the upper part of the bubble has a higher collapse velocity and causes a stronger disturbance in the flow field; the value of p_m near the bubble top will be higher. At later stage of the bubble collapse (frame d_2), a high-speed liquid jet forms and the maximum value of p_m is reaches 5.5. Therefore, the localization feature of p_m has greatly influenced the total pressure, as shown in frame d_1. Compared with p_m, the distribution of p_g is relatively symmetrical in spite of the non-spherical bubble shape.

In addition, it is noted that the jet in experiment is thinner than that of the numerical result. Philipp and Lauterborn (1998) illustrated that the curved bubble-liquid interface acts as a divergent lens, so the jet inside the bubble appears smaller by a factor of 1.33. Therefore, our numerical results meet the experimental results well in pre-toroidal bubble phase.

3.2.2 Toroidal bubble phase

A toroidal bubble forms after the jet penetrates the lower bubble surface. The numerical results of the toroidal bubble phase are shown in Fig. 5. These four moments corresponds to frames 5-8 in Fig. 3, respectively.
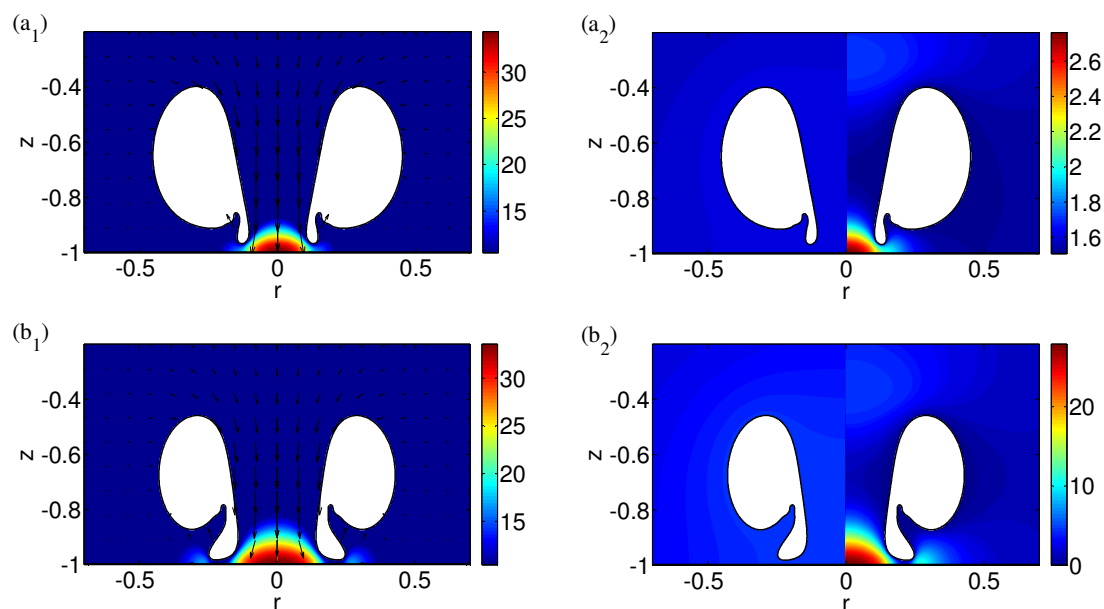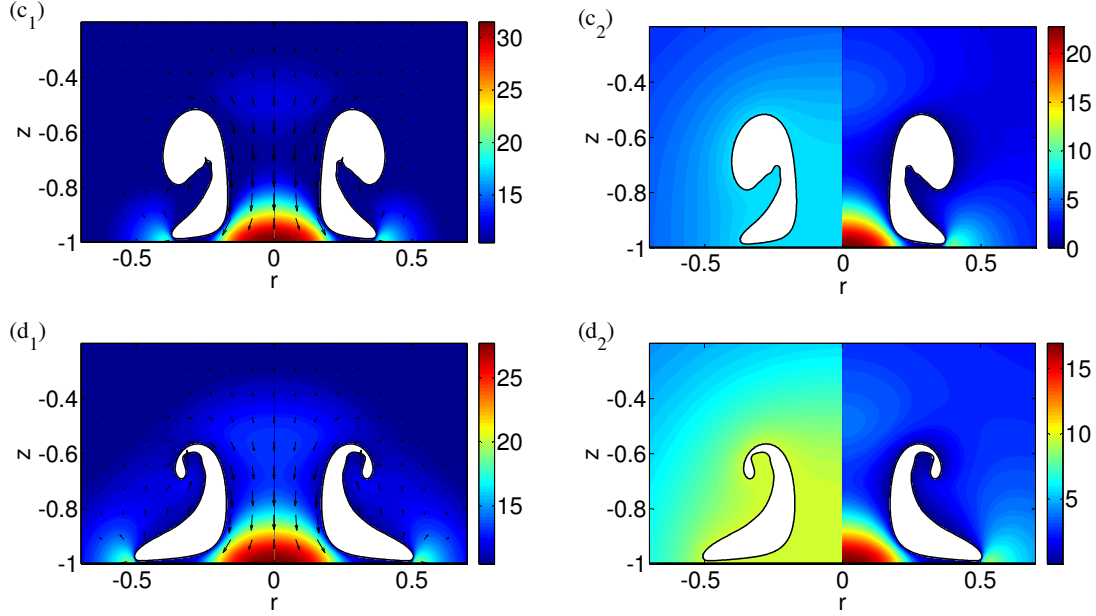
Fig. 5. Toroidal bubble dynamics near a rigid boundary for $\varepsilon = 50$, $\gamma = 1$, $\delta = 0.04$. The nondimensional times are 2.35, 2.38, 2.41 and 2.44, respectively. The location of the rigid boundary is the lower limit of the frames. The contours in left column represent p, and the right column represents p_g (on the left-half part) and p_m (on the right-half part).

In the left column of Fig. 5, the pressure contours and velocity fields surrounding the toroidal bubble are shown. A thin protrusion appears at the jet tip soon after the jet impact. The high-speed liquid jet impacts on the rigid wall and a stagnation point at the wall center is formed, generating a highly concentrated pressure region at the wall center (frame a_1). This phenomenon is significant in assessing possible mechanisms for structural damage due to cavitation, cleaning and underwater explosion. The area of this high pressure region increases as the width of the jet increases (frames b_1-d_1). Due to the restriction of the rigid wall and the high pressure at the wall center, the protrusion is redirected from the vertical direction to the radial direction (frames b_1-d_1). Meanwhile, an outward radial flow forms after the downward vertical jet flow impact on the wall. The annular high pressure region around the toroidal bubble is caused by the radial flow along the solid surface collides with the outside flow (frames c_1-d_1). The variations of the pressures on the wall versus time will be discussed in Section 3.2.4. We can also notice that an annular jet (sideways jet) is generated between the protrusion and the primary bubble surface (frame a_1), and travelling along the toroidal bubble surface upward (frames b_1-c_1), and making a collision with the other side of the bubble

(frames d_1). The splitting of a toroidal bubble is followed afterwards, which will be discussed in Section 3.2.3.

As shown in the right column of Fig. 5, the features of p_g in the toroidal bubble phase are similar to those in pre-toroidal bubble phase. The toroidal bubble keeps shrinking and the centroid of the bubble moves towards the wall gradually. It is clearly that the maximum value of p_g in the flow keeps increasing. The main feature of p_m induced by a toroidal bubble is the high pressure region located at the wall center, which is caused by the jet impact. The maximum pressure of p_m decreases gradually, indicating the decrease of the 'jet power'. In addition, the high pressure region of p_m above the bubble still exists. Although the pressure magnitude therein is much smaller than that around the wall center, this high pressure region acts like an engine driving the liquid jet impact on the rigid wall continuously. At last, the evolution of toroidal bubble shapes in calculation shows favorably agreement with the experimental images.

3.2.3 Toroidal bubble splitting phase

In Fig. 3 (frame 10), the splitting of the toroidal bubble can be observed. The real time of the splitting may be earlier because of observation difficulty due to the rough bubble surface. The numerical calculation predicts the splitting time is 2.446. The afterward numerical results are shown in Fig. 6.
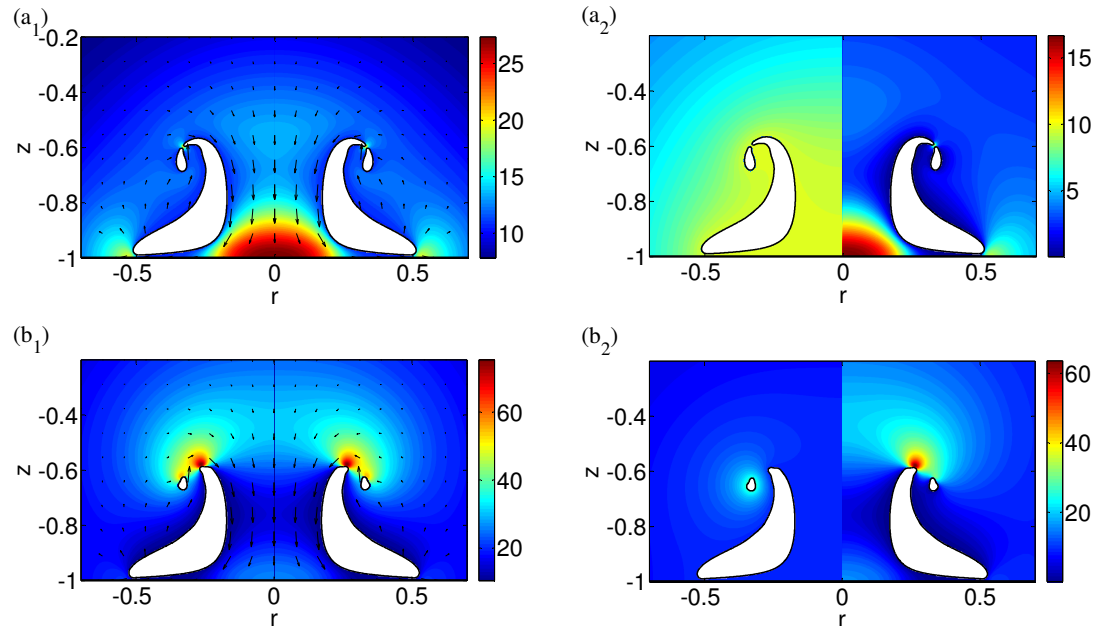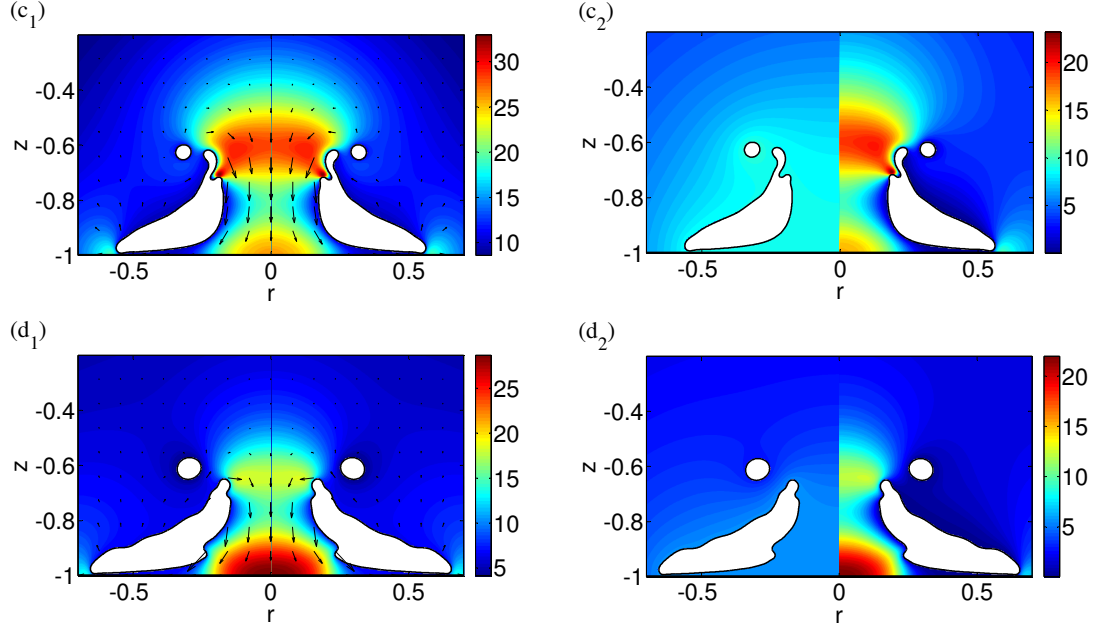
Fig. 6. The velocity fields and pressure contours in the flow after the toroidal bubble splitting near a rigid boundary for $\varepsilon = 50$, $\gamma = 1$, $\delta = 0.04$. The nondimensional times are 2.446, 2.450, 2.460 and 2.484, respectively. The location of the rigid boundary is the lower limit of the frames. The contours in left column represent p, and the right column represents p_g (on the left-half part) and p_m (on the right-half part).

In the left column of Fig. 6, the pressure contours and velocity fields around the two toroidal bubbles are shown. After the splitting, an annular high pressure region is generated at the splitting location (frame a_1). Zhang et al. (2015b) demonstrated that the maximum pressure at the splitting location is associated with the velocity differences between the two sides therein just before splitting. Then, a new annular jet propagates along the lower toroidal bubble (frame b_1-d_1), and the upper toroidal bubble keeps oscillating with a much shorter period.

In the right column of Fig. 6, p_g after the toroidal bubble splitting is shown on the left-half part. The toroidal bubble is rebounding just before the splitting. However, the lower one keeps rebounding while the upper one collapses after splitting. Similar phenomenon can also be found in Brujan et al. (2002) and Zhang et al. (2015b). Therefore, p_b of the two bubbles will differ from each other afterwards. p_g around the upper bubble is much higher than that around the lower one when the upper bubble reaches its minimum volume (frame b_2). After that, p_g around the upper bubble decreases as it rebounds (frame c_2) and over-expanded (frame d_2). The oscillations of

smaller bubble around a much larger bubble may contribute to a local high pressure region or shock wave emission Brujan et al. (2011) . As to p_m, the high pressure around the wall center still exists, indicating the main jet is still impacting on the wall (frames a_2-c_2), but the maximum pressure is decreasing. Besides, the annular sideways jet is accompanied with an annular high pressure region (frame b_2), moving downward towards the wall at t = 2.46 (frame c_2) and impacting on the wall at t =2.484 (frame d_2).

In this toroidal bubble splitting phase, compared with the experimental results, although a perfect fit is not to be expected, as the initial conditions cannot be specified to sufficient accuracy and some simplifications of the numerical model, the overall agreement is remarkable. From the discussion above, it is concluded that the emergence of the localized high pressure regions are caused by the asymmetrical motion of the bubble and has no connection with the inner gas pressure.

3.2.4 More discussion

The evolutions of p, p_g and p_m at the wall center and p_b versus time are plotted in Fig. 7. The evolutions of p_g and p_b have same patterns and they reach their peaks at the same time. The peaks of p are closely associated with p_m. It is noted that p_m increases rapidly and reaches its first peak (marked as A in Fig. 7) after the jet threading the lower bubble surface. As shown in Fig. 8(a), the maximum pressure on the symmetry axis keeps increasing and moves towards the boundary (z = -1). It should be stated that the pressure on the wall is continuously changing over time in calculation. This is due to the assumption that the jet impact occurs at a single point in the vortex ring model (Wang et al., 1996). The corresponding numerical treatment has little effect on the whole domain and the pressure in the flow field varies continuously. As for a domain-cut approach (Best, 1991), the pressure experienced at the wall is increased by over 50% due to the impact, which might be caused by the deletion of more nodes at the jet impact area. In fact, the maximum velocity on the axis is decreasing after the jet threading the bubble, as shown in Fig. 8(b). Therefore, p and p_m will decrease after peak A for the decreasing of jet velocity. However, the toroidal bubble is moving towards the wall rapidly around the minimum bubble volume moment (Wang, 2014), so the whole bubble will get much closer to the wall, resulting in p and p_m rise again to peak B, as shown in Fig. 7.
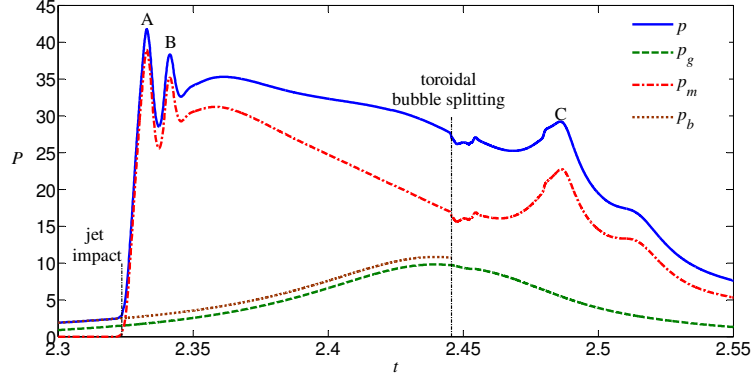
Fig. 7. Evolutions of p, p_g, p_m (at wall center) and p_b versus time.
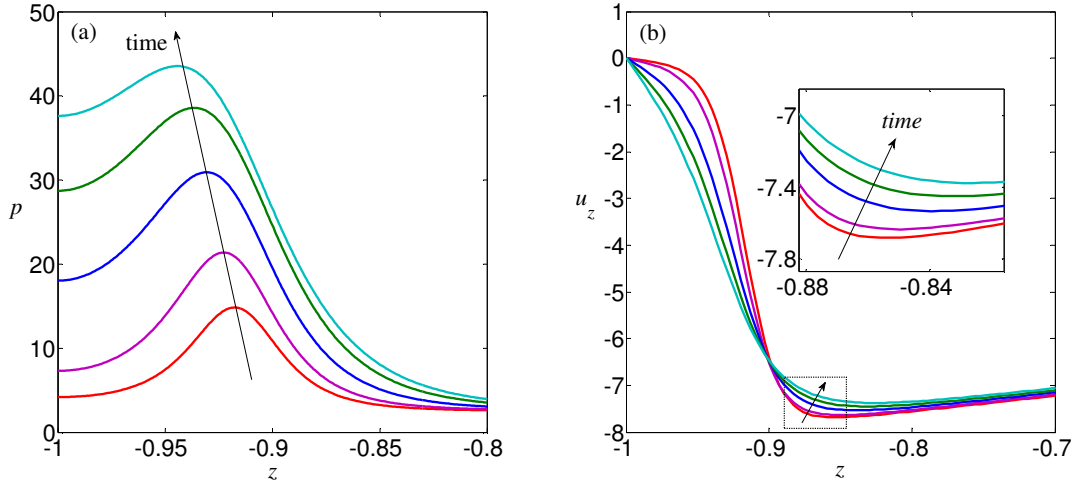

Fig. 8. The variations of the pressures and velocities on the symmetry axis of the toroidal bubble along the z-direction as shown in (a) and (b), respectively. The five times (t - t_{jet}) are 0.001, 0.002, 0.004, 0.006 and 0.008, respectively.

Back to Fig. 7, p and p_m decrease for the decreasing of jet velocity after peak B. During the splitting of the toroidal bubble, p and p_m still vary continuously except for a small fluctuation on the pressure curve. As mentioned above, an annular high pressure region is generated at the splitting location, which would influence the pressure on the wall more or less. Choi and Chahine (2004) also found that some noise is emitted after a bubble splitting. Besides, the topology treatment may also contribute to the instability of toroidal bubble dynamics. Another pressure peak emerges after the toroidal splitting, marked as C in Fig. 7. This pressure peak is associated with the annular jet propagation as mentioned in Section 3.2.3 (Fig. 6, frame d). As the rebounding of the lower toroidal

bubble, p, p_g and p_m decrease gradually.

The two decomposed pressure, p_g and p_m, in this case can be treated as the pressure pulse caused by the high pressure gas and the jet impact pressure. At the wall center, the maximum value of p_m is much higher than p_g. Meanwhile, the duration of p_m with higher pressure is longer than that of p_g. Therefore, the jet impact would cause much more damage at the wall center than the compressed gas in this case.

3.3 Effect of γ

As shown in previous studies, the non-dimensional stand-off parameter, γ, plays a very important role in bubble dynamics and the pressure on the wall. Besides, obvious damage is observed when γ is less than 2 in experiments (Philipp and Lauterborn, 1998). Bubbles in the range $1 \leq \gamma \leq 2$ are investigated in the present study. Fig. 9~Fig. 12 show four calculated results, corresponding to $\gamma = 1.2$, $\gamma = 1.4$, $\gamma = 1.6$ and $\gamma = 2$, respectively. And the strength parameters are all taken as 50 and buoyancy parameter zero. In addition, the time histories of p, p_g and p_m at the wall center and p_b of four cases are plotted in Fig. 13.
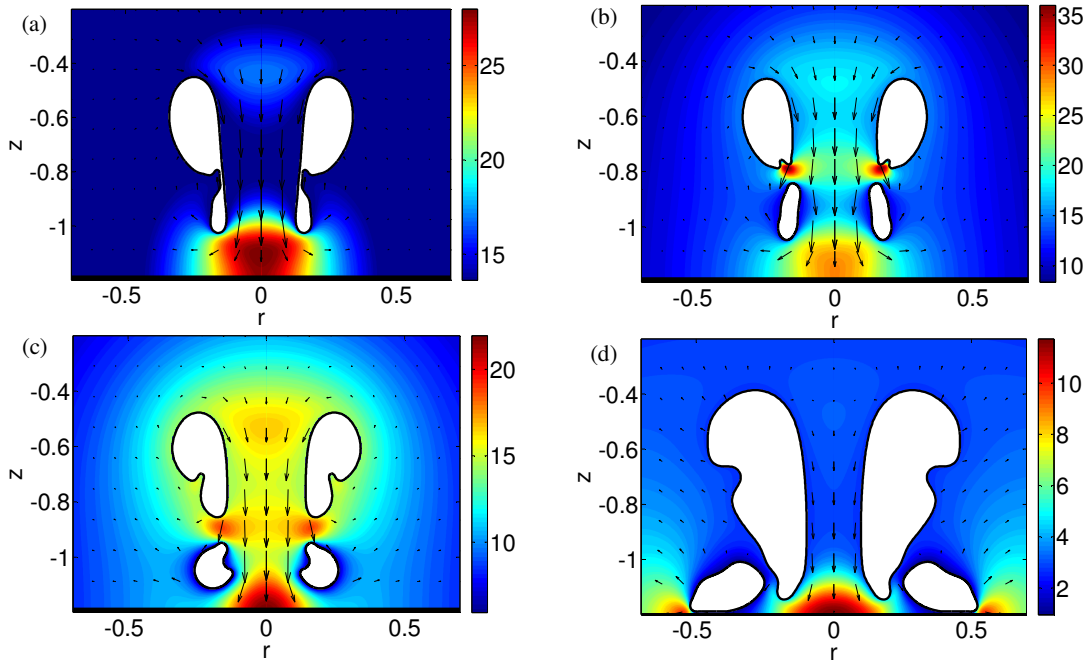

Fig. 9. Toroidal bubble dynamics near a rigid boundary for $\varepsilon = 50$, $\gamma = 1.2$, $\delta = 0$. The nondimensional times are 2.36, 2.37, 2.4 and 2.5, respectively. The location of the rigid boundary is the lower limit of the frames.

Fig. 9 shows the bubble shapes, pressure contours and velocity fields for $\gamma = 1.2$. Toroidal bubble splitting occurs after the jet impact, shown in frame (a). Similar phenomenon can also be found in Tong et al.'s (1999) experiment and numerical simulation. However, their calculation stopped at the splitting moment. Two toroidal bubbles form after the splitting and an annular high pressure region is generated at the splitting location, shown in frame (b). The high pressure region around the wall center still exists except for a reduction in maximum pressure value. Then, the lower toroidal bubble began to rebound and keeps moving towards the wall, as shown in frame (c). Meanwhile, the upper toroidal bubble continues shrinking and a new downward protrusion appears on its lower side. In addition, the pressure around the upper bubble is higher than that of the lower bubble. This is because the inner gas pressures of these two bubbles at this moment are 14.4 and 5.9, respectively. In frame (d), the upper toroidal bubble is rebounding and its lower protrusion has been drawn downward to the wall. The high pressure caused by the jet is contact with the wall, and the maximum pressure has decreased to 11.8. The lower toroidal bubble is moving outward along the wall and the annular high pressure region appears around the toroidal bubble, in which the maximum pressure is about 10.

The time histories of p, p_g and p_m at the wall center and p_b of this case are plotted in Fig. 13 (a). p_m increases rapidly and reaches its first peak (marked as A) soon after the jet impact. Then, another peak (marked as B) appears afterwards. This pattern is similar with the case in Section 3.2 and the cases discussed later. After the toroidal bubble splitting, p keeps rising with good continuity. However, there is an inflection on the p_g curve at the splitting moment. This can be explained as follows: the lower toroidal bubble rebounds after the splitting and migrates towards the wall, resulting in the reduction of its inner gas pressure and p_g. p_m and p reach their maximum value around $t = 2.41$, which is associated with the migration of the toroidal bubbles and the jet impact on the wall directly. On the whole, the jet plays a more important role than the gas pressure on the dynamic pressure in this case. In the experimental case ($\gamma = 1$), the smaller toroidal bubble after splitting is relatively far from the wall, so the splitting has little effect on the variation of p_g, as shown in Fig. 7.
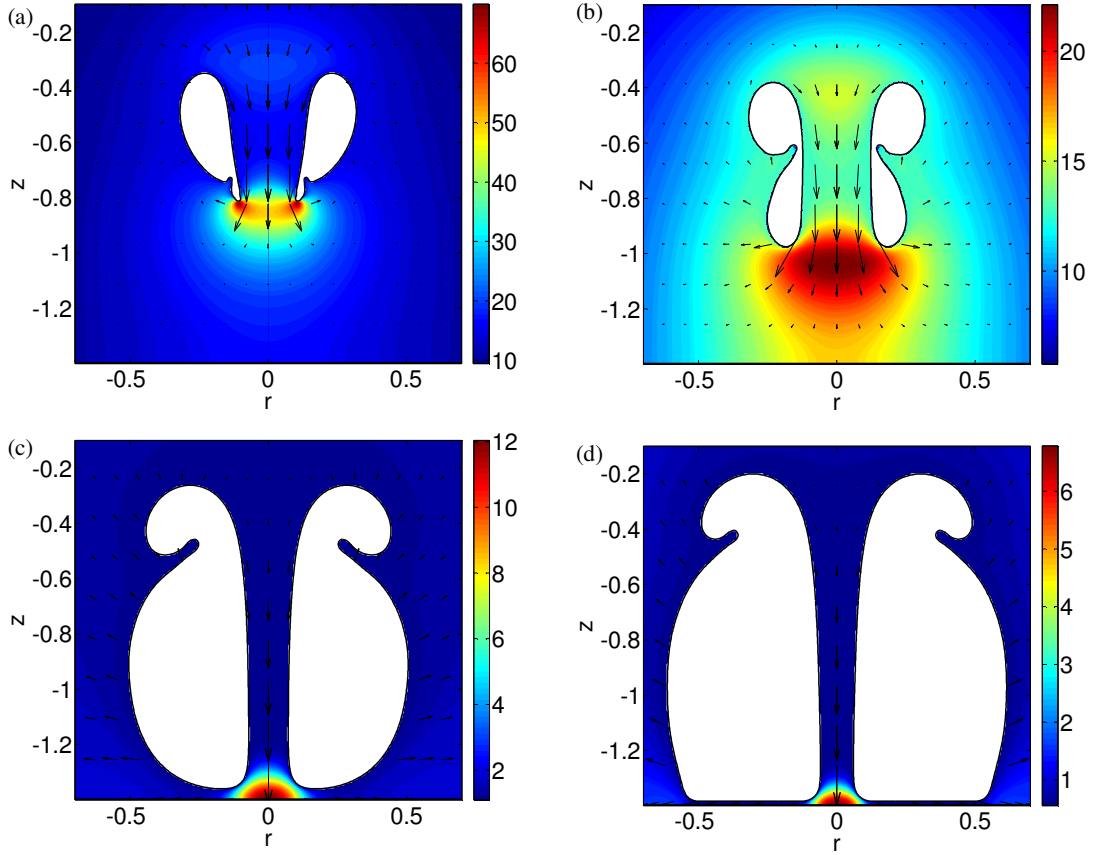
Fig. 10. Toroidal bubble dynamics near a rigid boundary for $\varepsilon = 50$, $\gamma = 1.4$, $\delta = 0$. The nondimensional times are 2.305, 2.35, 2.5 and 2.6, respectively. The location of the rigid boundary is the lower limit of the frames.

Fig. 10 shows the numerical results for $\gamma = 1.4$. The high pressure region caused by the jet is relatively far from the wall soon after the jet threading the bubble (frame a). As the toroidal bubble rebounds and migrates towards the wall, the high pressure region is also approaching the wall, but the magnitude and area of the pressure region are decreasing, as shown in frame b-d. The time histories of p, p_g and p_m at the wall center and p_b of this case are plotted in Fig. 13 (b). It is clear that p_g and p_b have the same variation pattern. The maximum p_g reaches 10.74, which is higher than the jet impact pressure (p_m at peak A equals 9.1). In this case, the water layer between the bubble and the wall is relatively thicker than the above cases, so the jet would be decelerated a lot and the jet impact pressure on the wall is reduced. As the toroidal bubble migrates towards the wall further, p_m increases relatively slow afterwards and reaches its maximum around $t = 2.5$. There is no splitting in this case. We find that the splitting phenomenon has close connection with the stand-off parameter. It is easier

for a toroidal bubble to split when γ is small. If ε is fixed as 50 and $\delta = 0$, the toroidal bubble splitting occurs when $\gamma \leq 1.3$. Besides, the strength parameter also has influence on the splitting, which will be discussed in the next section.
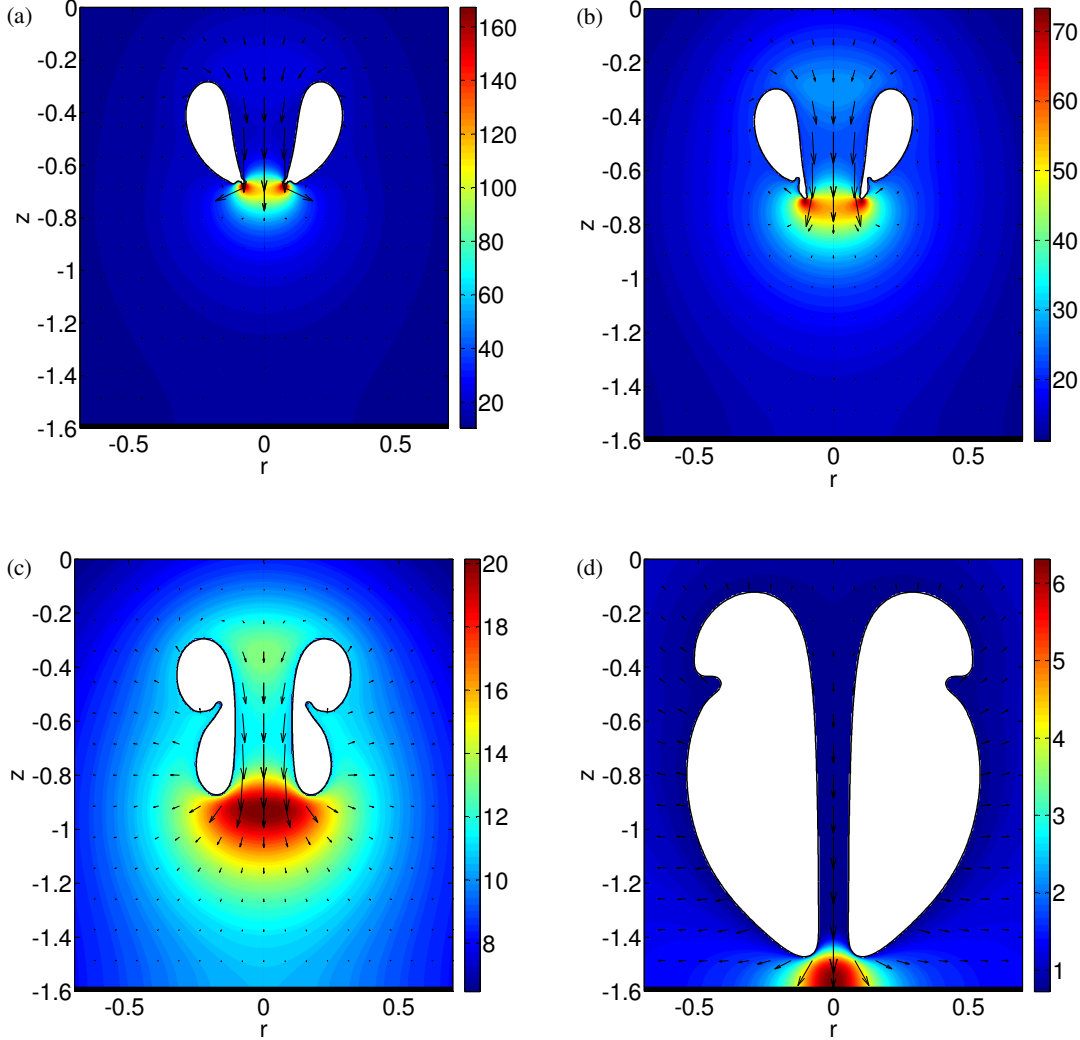

Fig. 11. Toroidal bubble dynamics near a rigid boundary for $\varepsilon = 50$, $\gamma = 1.6$, $\delta = 0$. The nondimensional times are 2.271, 2.279, 2.32 and 2.5, respectively. The location of the rigid boundary is the lower limit of the frames.

Fig. 11 shows the numerical results for $\gamma = 1.6$, which are similar with that for $\gamma = 1.4$. The evolutions of p, p_g and p_m at the wall center and p_b of this case are plotted in Fig. 13 (c). The maximum value of p_g and p_m are 9.5 and 6.3, respectively, indicating the pressure pulse induced by the gas pressure is higher than the jet impact pressure in this case. During the migration of the toroidal bubble, maintains a relatively stable
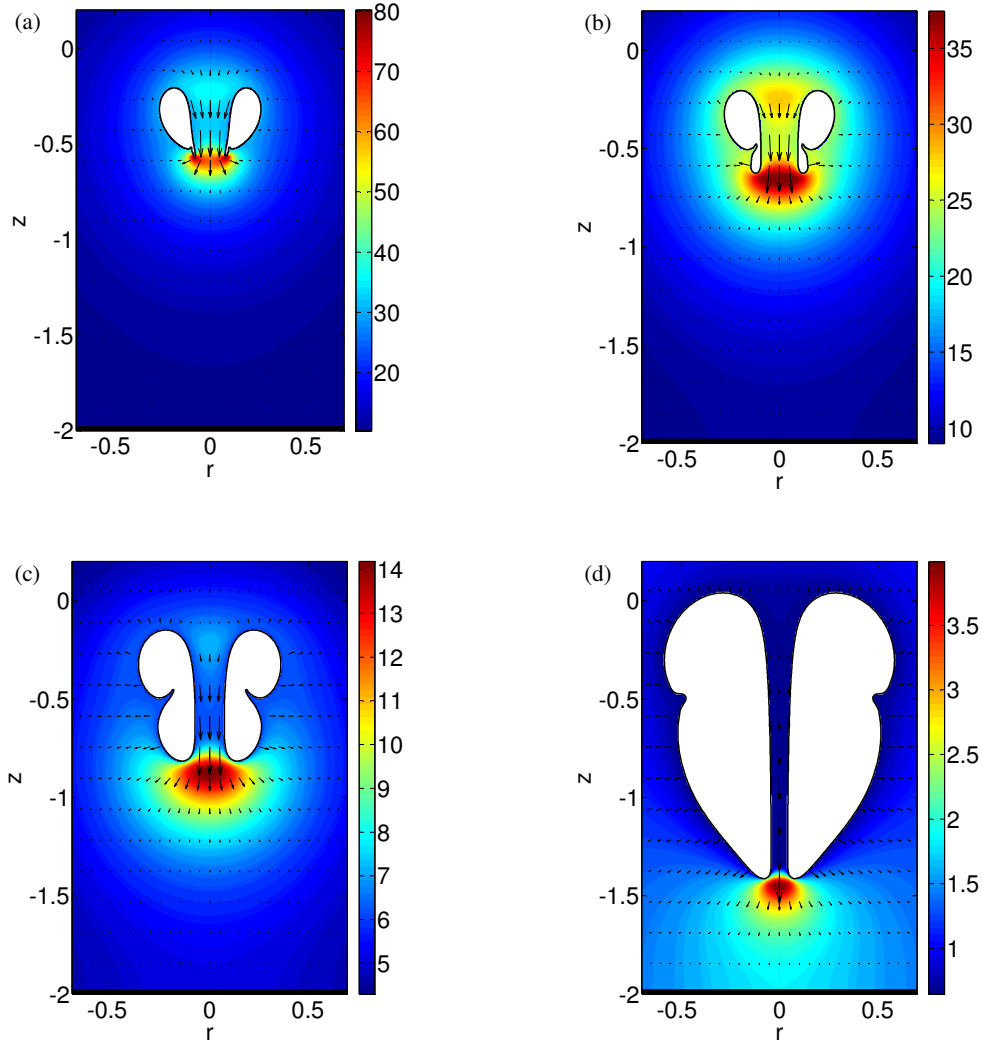
value first, and then increases slightly.

Fig. 12. Toroidal bubble dynamics near a rigid boundary for $\varepsilon = 50$, $\gamma = 2$, $\delta = 0$. The nondimensional times are 2.237, 2.25, 2.29 and 2.45, respectively. The location of the rigid boundary is the lower limit of the frames.

The numerical results for $\gamma = 2$ are shown in Fig. 12. The toroidal bubble motion and the pressure contours are similar with the above two cases. The evolutions of p, p_g and p_m at the wall center and p_b of this case are plotted in Fig. 13 (d). The maximum p_m is only 2.7, but the maximum p_g reaches 8.1. The gas pressure dominates the dynamic pressure on the wall in this case, and the jet impact plays a minor role.
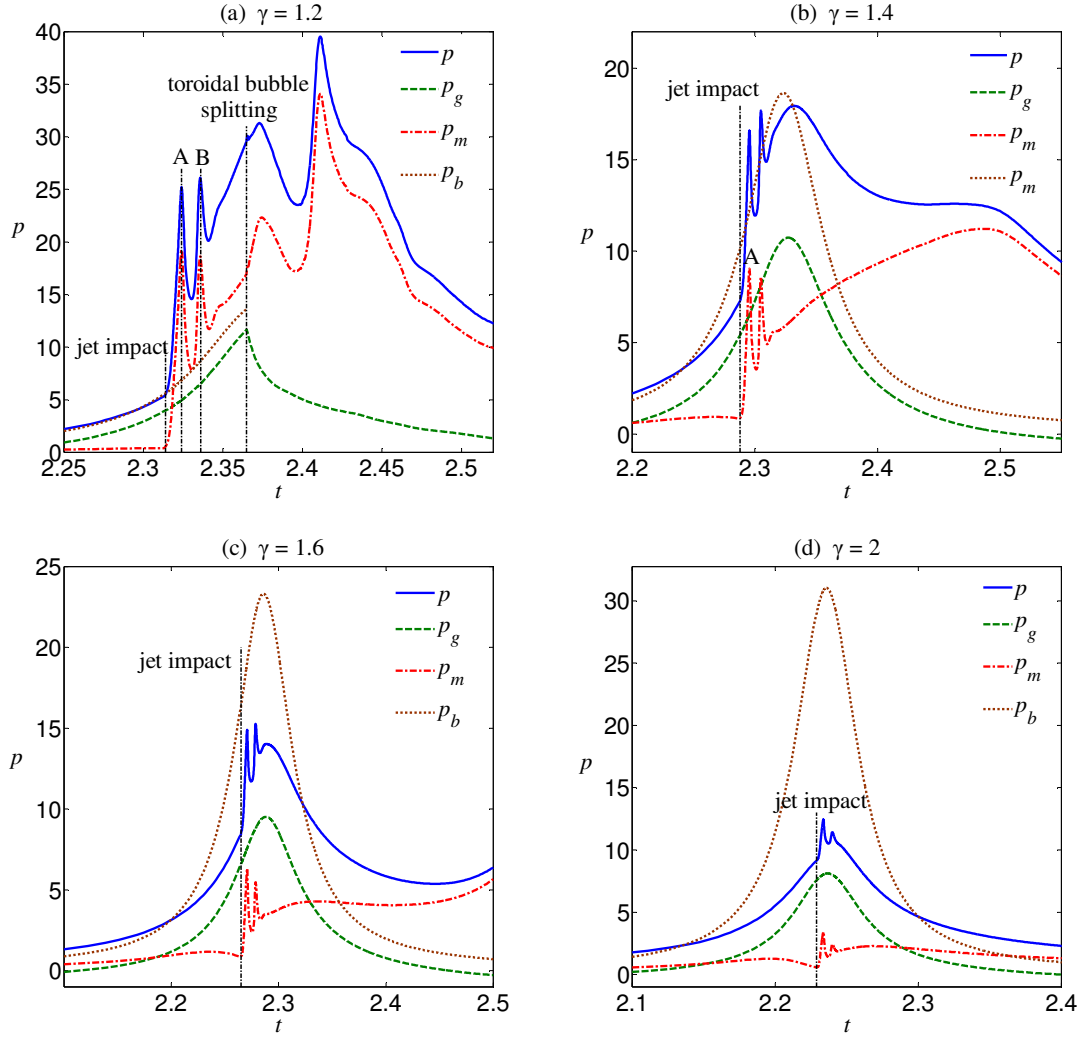
Fig. 13. Evolutions of p, p_g, p_m (at wall center) and p_b versus time. (a) $\gamma = 1.2$, (b) $\gamma = 1.4$, (c) $\gamma = 1.6$, (d) $\gamma = 2$.

From the cases discussed above, it is inferred that the stand-off parameter has great influence on both p_g and p_m. In order to investigate the effect of γ systemically, more cases are calculated. The maximum of p, p_g, p_m and p_b versus γ are plotted in Fig. 14. The maximum of p_m is taken as the first peak after the jet impact.
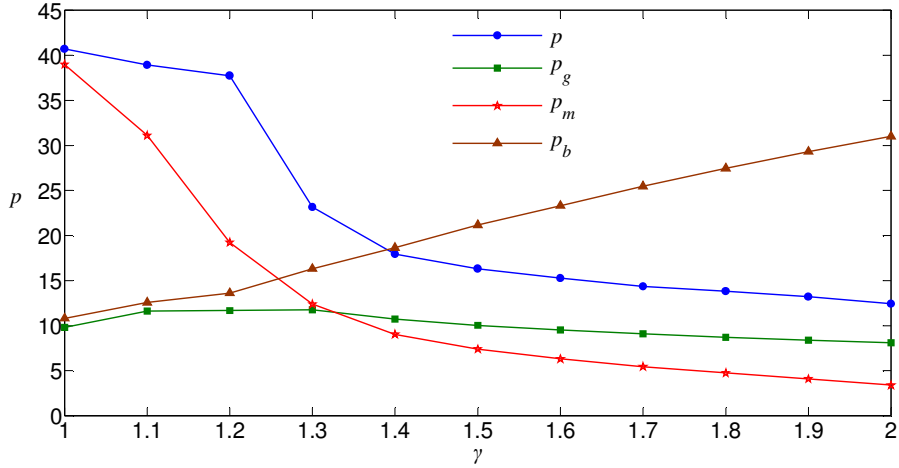
Fig. 14 The variations of the maximum value of p, p_g, p_m and p_b versus γ. Other parameters are taken as $\varepsilon = 50$, $\delta = 0$.

As shown in Fig. 14, p and p_m are both decreasing as γ increases from 1 to 2. The reduction of p varies relatively slow when $1 \le \gamma \le 1.2$ and $1.4 \le \gamma \le 2$. In the range of $1.2 \le \gamma \le 1.4$, p decreases relatively faster due to the increasing of γ and the splitting may also affect the variation of dynamic pressure. p_m decreases rapidly as γ increases from 1 to 1.4, indicating the jet impact pressure is obviously weakened as the thickness of the water layer between the bubble and the wall increases. p_g increases as γ increases from 1 to 1.3, and then decreases as γ increases from 1.3 to 2. This is because the bubble gains a higher inner gas pressure with a larger γ. There existing a critical γ that p_g gains a maximum.

The relationship of peak values between p_g with p_m varies versus γ. There exists a critical stand-off parameter, γ_c. If $\gamma < \gamma_c$, then $p_g < p_m$; else if $\gamma > \gamma_c$, then $p_g > p_m$. When ε is fixed as 50, γ_c is around 1.33.

3.4   Effect of ε

In this section, the effect of the strength parameter on pressure field will be investigated. In the first series of calculations, we fix γ as 1.5 and fix δ as 0. ε is ranging from 20 to 200.
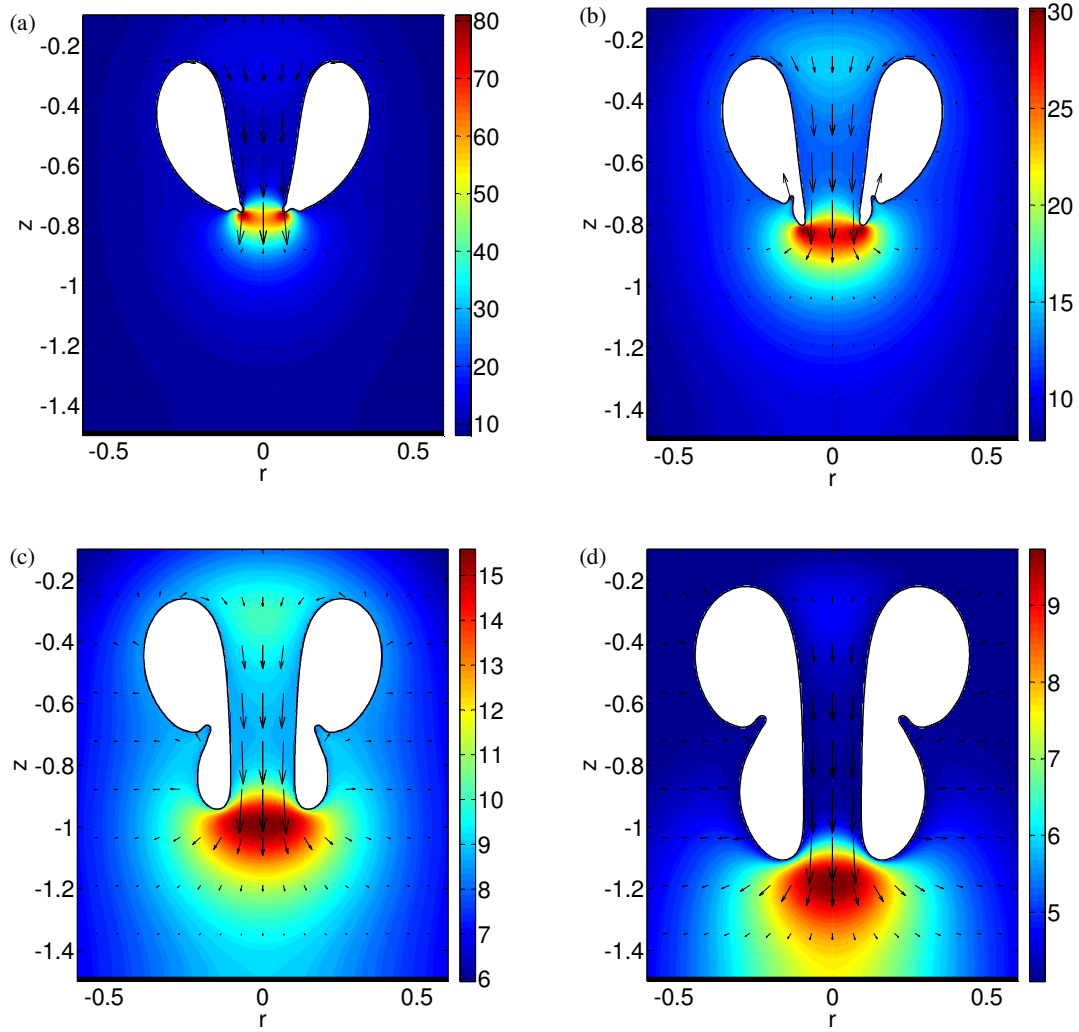
Fig. 15. Toroidal bubble dynamics near a rigid boundary for $\varepsilon = 20$, $\gamma = 1.5$, $\delta = 0$. The nondimensional times are 2.398, 2.41, 2.45 and 2.5, respectively. The location of the rigid boundary is the lower limit of the frames.

Fig. 15 shows the numerical results for $\varepsilon = 20$. The toroidal bubble rebounds soon after the jet impact. The high pressure region caused by the jet impact is moving towards the wall during the bubble migration. The maximum pressure therein decreases during the rebounding process of the bubble.
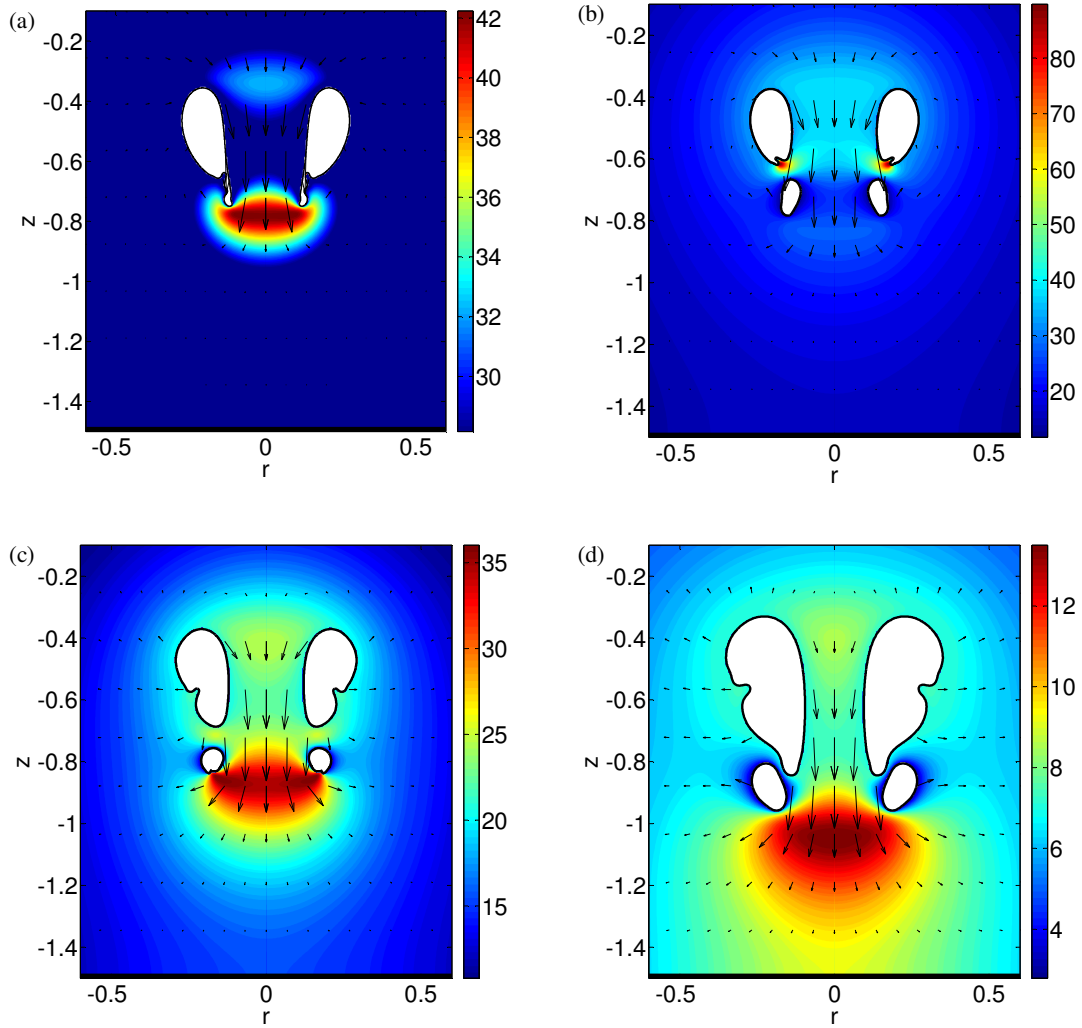
Fig. 16 Toroidal bubble dynamics near a rigid boundary for $\varepsilon = 100$, $\gamma = 1.5$, $\delta = 0$. The nondimensional times are 2.24 2.25, 2.27 and 2.3, respectively. The location of the rigid boundary is the lower limit of the frames.

Fig. 16 shows the numerical results for $\varepsilon = 100$. The toroidal bubble keeps shrinking after the jet impact, followed by the splitting of the toroidal bubble. Both the two toroidal bubbles migrate towards the wall after the splitting. The high pressure region caused by the main jet always exists and its magnitude decreases gradually. In this series of calculations, it is found that the splitting of the toroidal bubble occurs when $\varepsilon \geq 90$.

In the second series of calculations, we fix γ as 2 and fix δ as 0. The strength parameter is ranging from 20 to 300. The splitting of the toroidal bubble occurs when

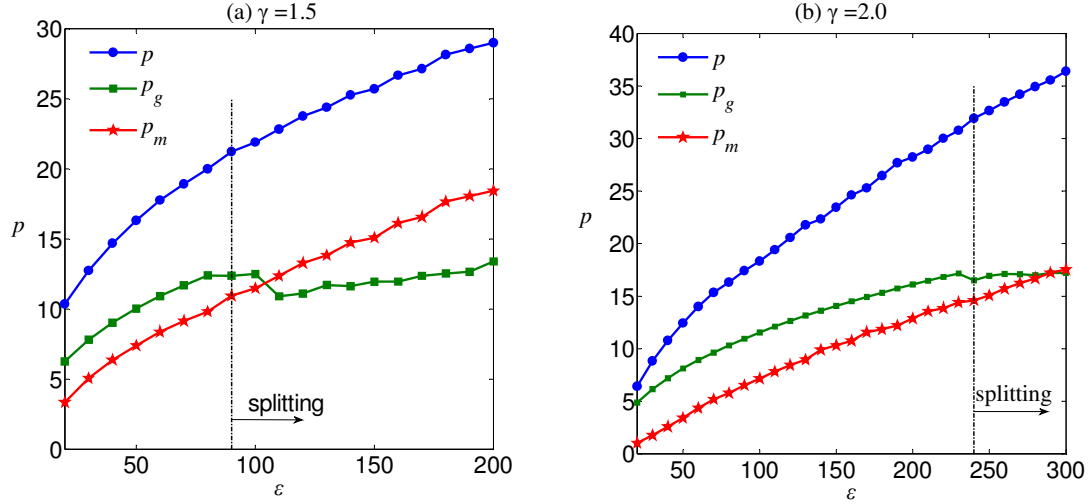$\varepsilon \geq 240$. In these two series of calculations, the variations of the maximum value of p, p_g and p_m versus ε are plotted in Fig. 17.

Fig. 17 The variations of the maximum value of p, p_g and p_m versus ε. Buoyancy parameter δ is taken as 0. (a) $\gamma = 1.5$, (b) $\gamma = 2$.

In Fig. 17, the maximum of p and p_m are increasing with ε, and the maximum of p_g also increases with ε except for a little reduction due to the splitting. The jet velocity increases as ε increases, resulting in a higher jet impact pressure. The splitting of the toroidal bubble weakens p_g. Compare p_g with p_m in Fig. 17 (a), it is noted that $p_g > p_m$ when $\varepsilon < 104$, and $p_g < p_m$ when $\varepsilon > 104$. Obviously, the strength parameter has great influence on the relationship between p and p_m. There also exists a critical strength parameter, ε_c. For a certain γ, if $\varepsilon < \varepsilon_c$, then $p_g > p_m$. As shown in Fig. 17 (b), ε_c is around 290 if $\gamma = 2$.

3.5   Effect of κ

The bubble gas is assumed adiabatic throughout the bubble life. The gas pressure is not only associated with bubble volume, but also the ratio of the specific heats, κ. Therefore, the effect of κ is studied in this section. In the following, four cases are discussed with κ being 1.1, 1.2, 1.3 and 1.4, respectively. Other parameters are taken as $\varepsilon = 50$, $\gamma = 2$, $\delta = 0$.
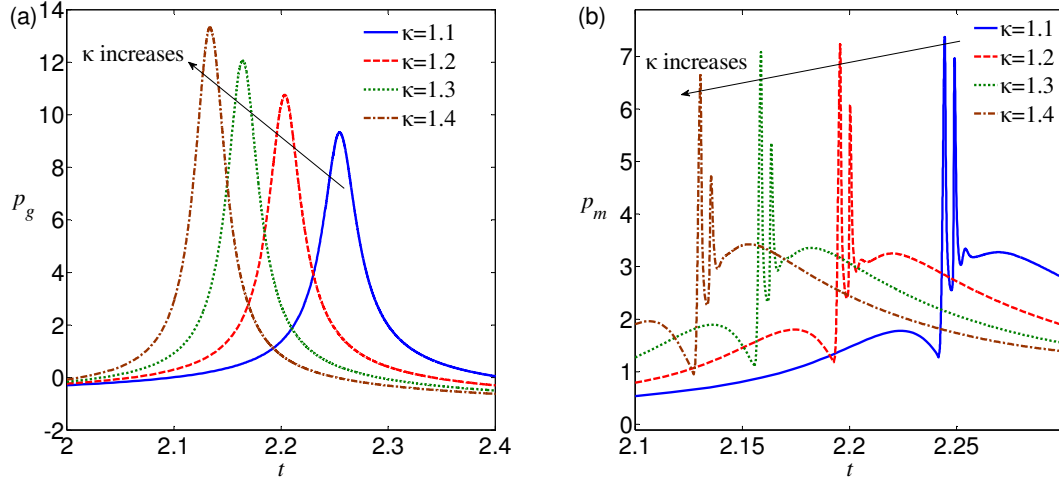
Fig. 18. The effect of κ on dynamic pressure at the wall center induced by a collapsing gas bubble for $\varepsilon = 50$, $\gamma = 2$, $\delta = 0$. (a) p_g, (b) p_m.

The variations of p_g and p_m at the wall center with different κ are shown in Fig. 18. The pressure curves are similar with each other except for the pressure peak and bubble oscillation period. As κ increases, the pressure peak of p_g increases and the bubble oscillation period decreases (shown in Fig. 18 (a)). On the contrary, pressure peak of p_m decreases as κ increases. It is inferred that the jet contains higher kinetic energy with a smaller κ. Through calculations, the kinetic energies at the jet impact moment of four cases are 1.01, 1.00, 0.96 and 0.90, respectively. Meanwhile, a higher kinetic energy indicates a lower potential energy and lower gas pressure of the bubble. Therefore, the pressure peak of p_g decreases when κ is decreasing.

3.6 The pressure induced by a cavitation bubble

The contents of a gas bubble (e.g. underwater explosion bubble) will not dissolve in the water at the collapse phase easily. We also ignore the mass transfer of a gas bubble in the above discussion. The formation of a cavitation bubble is usually due to the local pressure dropping below a critical pressure. Then, some micro-bubble nuclei in the flow grow explosively. When the ambient pressure around the cavitation bubble returns to a high value, the bubble will collapse and jet toward a nearby structure. Different from a gas bubble, the pressure inside a cavitation bubble is thought to be a constant (p_c) (Blake and Gibson, 1981; Blake et al., 1986).

In this section, the cavitation bubble is assumed to be initially a sphere of small

radius R_0, with its center located at the nondimensional distance γ above a rigid wall. The velocity potential on bubble surface at inception is given by Blake et al. (1986).

$$\varphi_0 = [\frac{2}{3}(R_0^{-3} - 1)]^{1/2}[1 + \frac{R_0}{((z+2\gamma)^2 + r^2)^{1/2}}] \tag{3.2}$$

In the following, two cases with different γ are discussed. The initial cavitation bubble radius keeps the same with the cases in Section 3.3. In the first case, the stand-off parameter is taken as $\gamma = 1$, and the pressure contours and velocity fields around the collapsing bubble are shown in Fig. 19. The jet velocity reaches 8.23 when the jet is impacting on the lower surface of the bubble (shown in Fig. 19 (a)), which is a 2.9% larger than that of a gas bubble in Fig. 4. This is because the gas pressure increases during the collapse phase of a gas bubble, therefore, the jet velocity would be decreased.
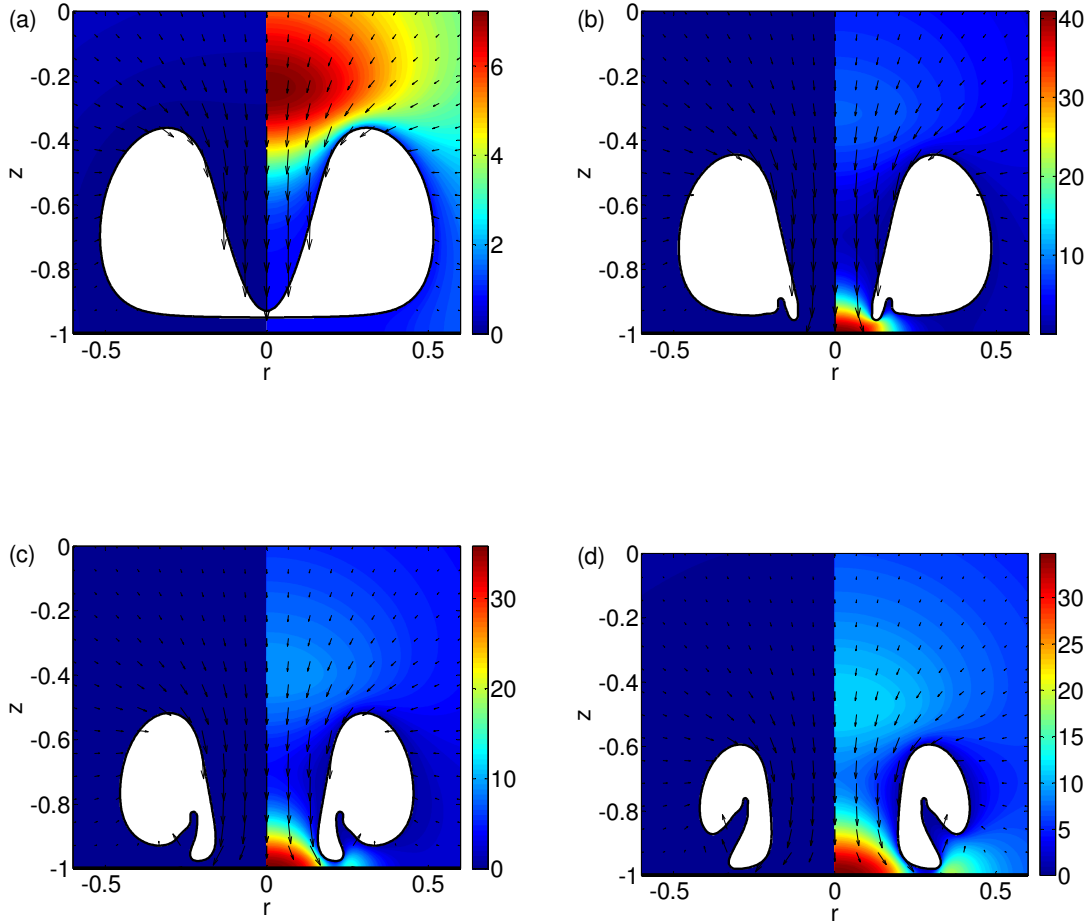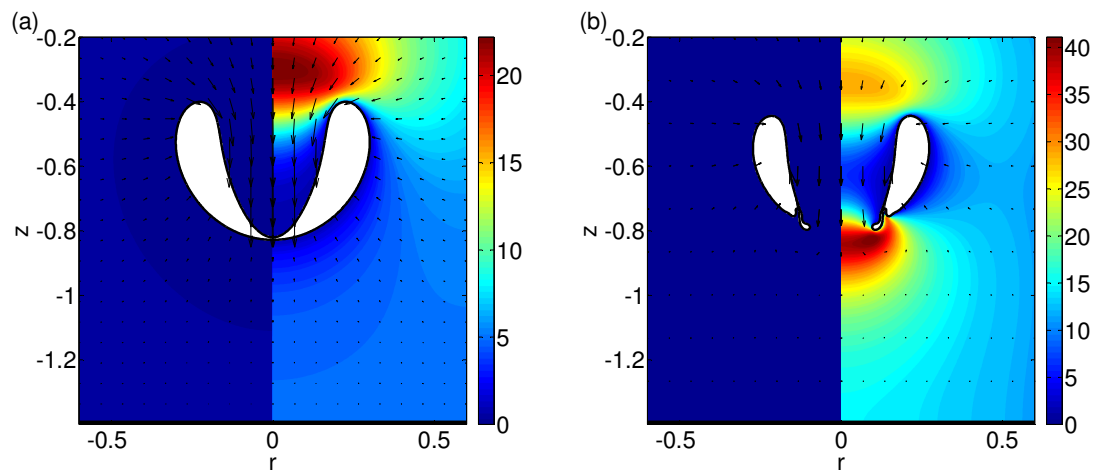
Fig. 19 The pressure induced by a cavitation bubble nearby a rigid boundary for $R_0 =$ 0.1911, $\gamma = 1$, $\delta = 0$. The nondimensional times are 2.18, 2.2, 2.22 and 2.24, respectively. p_g and p_m are shown on the left-half part the right-half part, respectively. The location of the rigid boundary is the lower limit of the frames.

Since the inner pressure of the cavitation bubble keeps p_c and always lower than the ambient pressure, p_g keeps negative during the whole process, as shown on the left-half part of Fig. 19. The distribution of p_m is similar with that of a gas bubble, as shown on the right-half part of Fig. 19. There exists a high pressure region above the bubble when the jet is forming (see Fig. 19 (a)). After the jet impact, another localized high pressure region is generated around the jet tip (see Fig. 19 (b)~(d)). The toroidal bubble keeps shrinking and the jet width is increasing and the maximum pressure decreases.
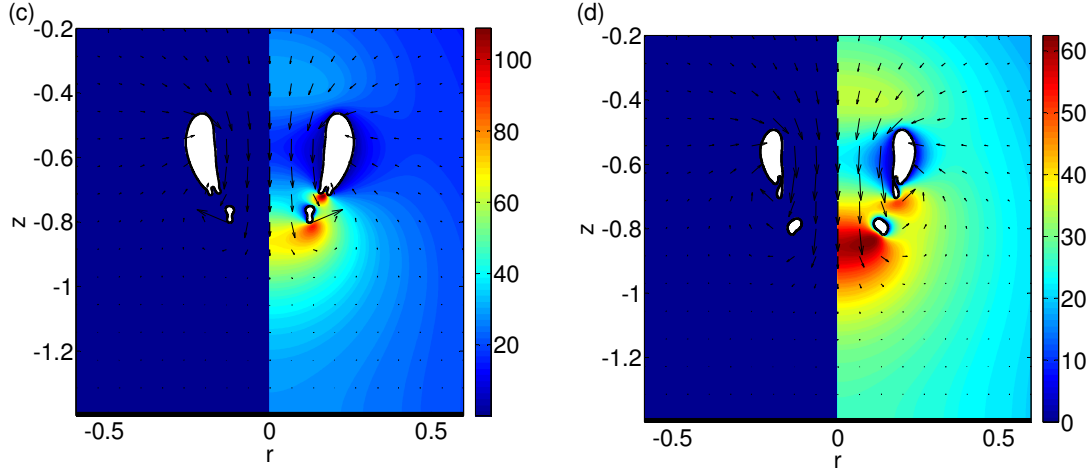
Fig. 20. The pressure induced by a cavitation bubble nearby a rigid boundary for $R_0 = 0.1911$, $\gamma = 1.4$, $\delta = 0$. The nondimensional times are 2.12, 2.127, 2.13 and 2.134, respectively. p_g and p_m are shown on the left-half part the right-half part, respectively. The location of the rigid boundary is the lower limit of the frames.

In the second case, the stand-off parameter is taken as $\gamma = 1.4$ and other parameters are the same with the first case. The pressure contours and velocity fields around the collapsing bubble are shown in Fig. 20. In this case, the jet velocity at the jet impact moment is 9.7, and the gas bubble jet velocity is 8.7 in the case of Fig. 10. p_g still keeps negative during the whole process and the distribution of p_m is always nonuniform. High pressure regions appear around the jet tip and splitting location. Different from the case in Fig. 10, the cavitation bubble splits during the toroidal bubble phase. However, the gas toroidal bubble rebounds and the split didn't occur (see Fig. 10).

Comparisons are made between cavitation bubble and gas bubble above; we can conclude that the jet velocity of cavitation bubble is higher than that of a gas bubble at the same γ. Besides, the cavitation bubble is easier to split. So there exist difference on dynamic behaviors of cavitation bubble and gas bubble. In addition, p_g induced by a cavitation bubble is always negative and p_m shows much similarity with the gas bubble.

3.7 Discusstion

The focus of this study is on the dynamic pressure generated by a single

collapsing bubble. However, bubbles do not exist in isolation in many practical situations and their dynamics show collective behavior due to inter-bubble interactions. Brujan et al. (2011, 2012, and 2014) studied the dynamics of bubble cloud near a rigid wall. They found the main mechanism of bubble clouds collapsing near a boundary is the high pressure generated inside the cloud at the minimum volume. Wijngaarden (2016) also demonstrated that one bubble may reinforce the neighboring ones during the cloud collapse, and the jets are less effective. Combine these arguments with the theory in this study, we may conclude that the high pressure induced by the bubble cloud is associated with the highly compressed bubble gas, and the jet impact plays a minor role. This is because the bubble cloud contains many small bubbles and most of them are relatively far from the boundary, so the micro-jets can't impact on the boundary directly and the bubble gas dominates the dynamic pressure. In certain circumstance, the bubble cloud collapses from the cloud surface and propagates inward, leading to strong energy focusing and a very high pressure inside the cloud (Brujan et al., 2012; Reisman et al., 1998). Therefore, those bubbles inside the cloud will be highly compressed and cause a higher pressure than an individual bubble. Nevertheless, the bubble cloud induced pressure still needs to be further investigated in the future.

4. Conclusions

The pressure field induced by a collapsing bubble near a rigid boundary is investigated in this study. Firstly, boundary element method is employed to simulate the bubble motion and the auxiliary function method is used to calculate the pressure field. Secondly, the dynamic pressure caused by bubble is decomposed into two parts; they are p_g caused by the imbalanced pressure between bubble gas and the ambient flow, and p_m related to the bubble motion. p_g and p_m are corresponding to the pressure pulse caused by bubble gas and the jet impact pressure respectively. The numerical results meet the experimental results well for both bubble shape evolution and pressure field. At last, the features of the two decomposed pressures caused by a gas/cavitation bubble are analyzed, and the effects of the stand-off parameter γ, the strength parameter ε and the ratio of the specific heats κ are also discussed in detail. The main conclusions could be made as follows.

1. p_g is almost uniformly distributed near the bubble surface. However, the p_m contour displays localized high pressure regions, located behind the bubble jet during the collapse phase and around the jet tip after jet impact.

2. The variations of p_g on the wall and the bubble gas pressure have the same variation pattern before bubble splitting. The splitting of the toroidal bubble will weaken p_g when the smaller sub-bubble is closer to the wall.

3. After jet impact, p_m on the wall increases rapidly and reaches its first peak, and then decreases due to the decrease of the jet velocity. The toroidal bubble will migrate towards the wall afterwards and p_m may rise again.

4. The maximum p_m decreases rapidly as γ increases from 1 to 1.4. There exists a critical stand-off parameter, γ_c. If $\gamma < \gamma_c$, the pressure on the wall is dominated by the jet impact; otherwise, the bubble gas dominates. If $\varepsilon = 50$ and $\delta = 0$, γ_c is around 1.33.

5. The maximum of p and p_m are increasing with ε, and the maximum of p_g also increases with ε except for a little reduction due to the splitting. For a certain γ, there also exists a critical strength parameter, ε_c. If $\varepsilon < \varepsilon_c$, $p_g > p_m$. ε_c is around 104 if $\gamma = 1.5$ and 290 if $\gamma = 2$.

6. As κ increases, the pressure peak of p_g increases and the pressure peak of p_m decreases.

7. The jet velocity of cavitation bubble is higher than that of a gas bubble at the same γ. Besides, the cavitation bubble is easier to split. p_g induced by a cavitation bubble is always negative and p_m shows much similarity with the gas bubble.

Acknowledgements

References

Best, J.P., 1991. The dynamic of underwater explosion. PhD Thesis, University of Wollongong, Australia.

Best, J.P., Kucera, A., 1992. A numerical investigation of non-spherical rebounding bubbles. J. Fluid Mech. 245, 137-154.

Best, J.P., 1993. The formation of toroidal bubbles upon the collapse of transient cavities. J. Fluid Mech. 251, 79-107.

Blake, J.R., Gibson, D.C., 1981. Growth and collapse of a vapour cavity near a free surface. J. Fluid Mech. 111, 123-140.

Blake, J.R., Taib, B.B., Doherty, G., 1986. Transient cavities near boundaries. Part 1. Rigid boundary. J. Fluid Mech. 170, 479-497.

Blake, J.R., Hooton, M.C., Robinson, P.B., Tong, R.P., 1997. Collapsing cavities, toroidal bubbles and jet impact. Phil. Trans. R. Soc. Lond. A. 355, 537-550.

Brujan, E.A., Nahen, K., Schmidt, P., Vogel, A., 2001. Dynamics of laser-induced cavitation bubbles near elastic boundaries: influence of the elastic modulus. J. Fluid Mech. 433, 283-314.

Brujan, E.A., Keen, G.S., Vogel, A., Blake, J.R., 2002. The final stage of the collapse of a cavitation bubble close to a rigid boundary. Phys. Fluids 14, 85-92.

Brujan, E.A., Ikeda, T., Yoshinaka, K., Matsumoto, Y., 2011. The final stage of the collapse of a cloud of bubbles close to a rigid boundary. Ultrason. Sonochem. 18, 59-64.

Brujan, E.A., Ikeda, T., Matsumoto, Y., 2012. Shock wave emission from a cloud of bubbles. Soft Matter 8, 5777-5783.

Brujan, E.A., Matsumoto, Y., 2014. Shock wave emission from a hemispherical cloud of bubbles in non-Newtonian fluids. J. Non-Newton Fluid Mech. 204, 32-37.

Chahine, G.L., Kapahi, A., Choi, J.K., Hsiao, C.T., 2016. Modeling of surface cleaning by cavitation bubble dynamics and collapse. Ultrason. Sonochem. 29, 528-549.

Choi, J.K., Chahine, G.L., 2004. Noise due to extreme bubble deformation near inception of tip vortex cavitation. Phys. Fluids 16, 2411-2418.

Choi, J.K., Hsiao, C.T., Chahine, G.L., Ceccio, G.L., 2009. Growth, oscillation and collapse of vortex cavitation bubbles. J. Fluid Mech. 624, 255-279.

Dadvand, A., Khoo, B.C., Shervani-Tabar, M.T., 2009. A collapsing bubble-induced microinjector: an experimental study. Exp. Fluids 46, 419-434.

Dadvand, A., Shervani-Tabar, M.T., Khoo, B.C., 2011. A note on spark bubble drop-on-demand droplet generation: simulation and experiment. Int. J. Adv. Manuf. Technol. 56, 245-259.

Dawoodian, M., Dadvand, A., Nematollahi, A., 2015. Simulation of bubble dynamics near a plate with an aperture in a vertical cylinder using a combined boundary element-finite difference method. Eng. Anal. Bound. Elem. 59, 187-197.

Duncan, J. H., Zhang, S., 1991. On the interaction of a collapsing cavity and a compliant wall. J. Fluid Mech. 226, 401-423.

Duncan, J.H., Milligan, C.D., Zhang, S.G., 1996. On the interaction between a bubble and a submerged compliant structure. J. Sound Vib. 197, 17-44.

Gibson, D. C., Blake, J. R., 1982. The growth and collapse of bubbles near deformable surfaces. Appl. Sci. Res. 38, 215-224.

Graaf, K.L., Penesis, I., Brandner, P.A., 2014. Modelling of seismic airgun bubble dynamics and

pressure field using the Gilmore equation with additional damping factors. Ocean Eng. 76, 32-39.

Han, R., Zhang, A.M., Liu, Y.L., 2015. Numerical investigation on the dynamics of two bubbles. Ocean Eng. 110, 325-338.

Harrison, M., 1952. An experimental study of single bubble cavitation noise. J. Acoust. Soc. Am. 24, 776-782.

Hsiao, C.T., Chahine, G.L., 2012. Effect of a propeller and gas diffusion on bubble nuclei distribution in a liquid. J. Hydr. Ser. B, 24, 809-822.

Klaseboer, E., Hung, K.C., Wang, C., Wang, C.W., Khoo, B.C., Boyce, P., Debono, S., Charlier, H., 2005. Experimental and numerical investigation of the dynamics of an underwater explosion bubble near a resilient/rigid structure. J. Fluid Mech. 537, 387-413.

Klaseboer, E., Turangan, C., Fong, S.W., Liu, T.G., Hung, K.C., Khoo, B.C., 2006. Simulations of pressure pulse–bubble interaction using boundary element method. Comput. Methods Appl. Mech. Engrg. 195, 4287-4302.

Liu, Y.L., Zhang, A.M., Tian, Z.L., 2014. Approximation of underwater explosion bubble by singularities based on BEM. Ocean Eng. 75, 46-52.

Naude, C.F., Ellis, A.T., 1961. On the mechanism of cavitation damage by non- hemispherical cavities in contact with a solid boundary. ASME J. Basic Eng. 83, 648–656.

Ohl, C.D., Arora, M., Dijkink, R., Janve, V., Lohse, D., 2006. Surface cleaning from laser-induced cavitation bubbles. Appl. Phys. Lett. 89, 074102.

Philipp, A., Lauterborn, W., 1998. Cavitation erosion by single laser-produced bubbles. J. Fluid Mech. 361, 75-116.

Rayleigh, L. VIII., 1917. On the pressure developed in a liquid during the collapse of a spherical cavity. Phil. Mag. 34, 94-98.

Reisman, G. E., Wang, Y. C., Brennen, C. E., 1998. Observation of shock waves in cloud cavitation. J. Fluid Mech. 355, 255-283.

Robinson, P.B., Blake, J.R., Kodama, T., Shima, A., Tomita, Y., 2001. Interaction of cavitation bubbles with a free surface. J. Appl. Phys. 89, 8225-8237.

Song, W.D., Hong, M.H., Lukyanchuk, B., Chong, T.C., 2004. Laser-induced cavitation bubbles for cleaning of solid surfaces. J. Appl. Phys. 95, 2952-2956.

Tinguely M., 2013. The effect of pressure gradient on the collapse of cavitation bubbles in normal and reduced gravity. PhD Thesis, ÉCOLE POLYTECHNIQUE FÉDÉRALE DE LAUSANNE, Switzerland.

Tong, R.P., Schiffers, W.P., Shaw, S.J., Blake, J.R., Emmony, D.C., 1999. The role of 'splashing' in the collapse of a laser-generated cavity near a rigid boundary. J. Fluid Mech. 380, 339-361.

Wang, C., Khoo, B. C., 2004. An indirect boundary element method for three-dimensional explosion bubbles. J. Comput. Phys. 194, 451-480.

Wang, Q.X., Yeo, K.S., Khoo, B.C., Lam, K.Y., 1996. Nonlinear interaction between gas bubble and free surface. Comput. Fluids 25, 607-628.

Turangan, C.K., Ong, G.P., Klaseboer, E., Khoo, B.C., 2006. Experimental and numerical study of transient bubble-elastic membrane interaction. J. Appl. Phys. 100, 054910.

Wang, Q.X., Yeo, K.S., Khoo, B.C., Lam, K.Y., 2005. Vortex ring modelling for toroidal bubbles. Theor. Comput. Fluid Dyn. 19, 303–317.

Wang, Q.X., 2013. Underwater explosion bubble dynamics in a compressible liquid. Phys. Fluids 25, 072104.

Wang, Q.X., 2014. Multi-oscillations of a bubble in a compressible liquid near a rigid boundary. J. Fluid Mech. 745, 509-536.

Wijngaarden, L.V., 2016. Mechanics of collapsing cavitation bubbles. Ultrason. Sonochem. 29, 524-527.

Wu, G.X., Hu, Z.Z., 2004. Simulation of non-linear interactions between waves and floating bodies through a finite-element-based numerical tank. Proc. R. Soc. Lond. A. 460, 2797–2817.

Zhang, A.M., Wang, C., Wang, S.P., Cheng, X. D., 2012. Experimental study of interaction between bubble and free surface. Acta Phys. Sin. 61, 084701.

Zhang, A.M., Wang, S.P., Huang, C., Wang, B., 2013a. Influences of initial and boundary conditions on underwater explosion bubble dynamics. Eur. J. Mech. B-Fluid. 42, 69-91.

Zhang, A.M., Xiao, W., Wang, S.P., 2013b. Experimental investigation of the interaction between a pulsating bubble and a rigid cylinder. Acta Mech. Sin. 29, 503-512.

Zhang, A.M., Cui, P., Cui, J., Wang, Q.X., 2015a. Experimental study on bubble dynamics subject to buoyancy. J. Fluid Mech. 776, 137-160.

Zhang, A.M., Li, S., Cui, J., 2015b. Study on splitting of a toroidal bubble near a rigid boundary. Phys. Fluids 27, 062102.

Zhang, A.M., Liu, Y.L., 2015. Improved 3d bubble dynamics model based on Boundary Element Method. J. Comput. Phys. 294, 208-223.

Zhang, S., Duncan, J., Chahine, G.L., 1993. The final stage of the collapse of a cavitation bubble near a rigid wall. J. Fluid Mech. 257, 147-181.